Ivânia Patrícia Rijo Trêpo Bate

Bachelor of Science in Micro and Nanotechnologies Engineering

Transparent and flexible ECoG electrode arrays of metallic nanostructures for neural recordings

Dissertation submitted in partial fulfillment of the requirements for the degree of
Masters in Micro and Nanotechnologies Engineering

Adviser: Dr. Joana Pereira Neto, Postdoctoral Research Associate, Nova University of Lisbon

Co-Adviser: Dr. Hugo Gravato Marques, Postdoctoral Researcher, Champalimaud Center for the Unknown

Examination Comittee

Chairperson: Prof. Dr. Rodrigo Ferrão de Paiva Martins, Full Professor, Nova University of Lisbon

Raporteur: Dr. Patrick Ruther, Group Leader – IMTEK, University of Freiburg

Member: Dr. Joana Pereira Neto, Postdoctoral Research Associate, Nova University of Lisbon

FACULDADE DE
CIÊNCIAS E TECNOLOGIA
UNIVERSIDADE NOVA DE LISBOA

June, 2021

Transparent and flexible ECoG electrode arrays of metallic nanostructures for neural recordings

Faculty of Sciences and Technology

Nova University of Lisbon

“Ninguém vence sozinho, nem no campo, nem na vida.”

- Papa Francisco

Acknowledgements

Este documento marca o passo final de um momento muito importante na minha vida: a conclusão do mestrado integrado. Gostaria de dizer que é o fim da minha escolaridade, mas não, porque sou uma eterna estudante. Todo o fim é um começo, e, como tal, prefiro ver este manuscrito como uma prova das minhas capacidades como futura profissional. Tudo isto não seria possível sem a ajuda de várias pessoas nas diferentes esferas da minha vida que de alguma forma contribuíram para que eu aqui chegasse.

Obrigada à Faculdade de Ciências e Tecnologia da Universidade Nova de Lisboa, a minha *alma mater* e segunda casa (ou talvez primeira?) nestes últimos anos. Ao DCM pela qualidade do ensino que me forneceu e ao meu Coordenador de Curso Professor Hugo Águas por me ajudar.

Um especial agradecimento à Professora Elvira Fortunato e ao Professor Rodrigo Martins por terem criado o meu curso, por me terem fornecido excelentes condições para desenvolver os meus trabalhos laboratoriais, tanto no CENIMAT|i3N como no CEMOP-UNINOVA, e por me inspirarem constantemente com as suas conquistas nacionais e internacionais.

Aos meus co-orientadores, Professor Pedro Barquinha e Dr. Hugo Marques, por terem aceitado este projeto, por confiarem em mim para desenvolver esta ideia, por partilharem tudo o que sabem comigo e sempre me darem os melhores conselhos.

Obrigada à minha *teache*r Joana Neto que me ensinou tudo o que está nesta tese e mais um pouco. Pela partilha de conhecimento, de experiências, de longas horas de laboratório e de câmara limpa, sempre acompanhadas de sentido de humor, de uma palavra amiga e do nosso lema “Se fosse fácil, todos faziam”.

Obrigada aos professores e investigadores do CENIMAT|i3N e CEMOP-UNINOVA Professora Joana Pinto, Ana Santa, Maria Pereira, André Moura, Tomás Calmeiro, Sirazul Haque e Miguel Alexandre que muito me ajudaram a entender e fazer todos os processos, e sempre se mostraram disponíveis para esclarecer qualquer dúvida.

Obrigada aos ratinhos por darem a sua vida, inconsciente e involuntariamente, em prol da minha tese e artigo, mas, mais importante, em prol do avanço científico.

Obrigada às minhas amigas Carol e Inês, que quando estamos juntas a casa vai literalmente abaixo. Ao Nuno na Terra Deus no Céu, ao Pitta e ao JP por todas as parvoíces durante o dia e relatórios durante a noite. Obrigada aos meus afilhados Luís, Bubu e Sara pela confiança depositada.

Obrigada a todos os meus amigos setubalenses Ana, às Kikas a dobrar e à Martinha; ao David, ao Chico, à Bia, ao Caniço, à Filipa, ao Coelho, ao Pina e aos primos Bruno e Joana; à Alex, à Cláudia e à Rita, as paramédicas mais engraçadas. Todos eles me recordam que, na minha pequena cidade, tenho efetivamente em cada esquina um amigo.

Obrigada aos meus tios Tininha e Zé Pinto, por estarem sempre presentes, e ao primo Flávio pelas conversas super interessantes que temos, e à tia Belinha. Aos meus tios Vasco e Caty que mesmo de longe se fazem sentir através de saudade, e aos meus dois priminhos Baptiste et Céleste, *mes chéris*. Também ao meu Martim, meu futuro guarda-costas profissional, que com metade da minha idade, já era maior que eu.

Obrigada aos meus tios Carlos e Fernando, e às tias doidas Guida e Ana. Obrigada aos meus primos Anita, André e Sílvia. Obrigada à minha querida madrinha Sandra, e primos Rodrigo, Didi e Miguel Ângelo.

Obrigada aos meus queridos avozinhos Tila, Rijo e Emília pela ternura e orgulho que sempre transluziu através das lentes dos óculos.

MUITO OBRIGADA às quatro pessoas mais chatas e com o maior coração do mundo: pai, mãe e manos. Conseguimos. Obrigada ao meu pai por ter abdicado do seu sonho de ser engenheiro para poder dar esse mesmo sonho aos seus três filhos, com muito esforço e sacrifício. Não sabes o quanto te admiro por ver a tua dor, e saber que é grande, mas por ver a tua coragem, e saber que é maior ainda. Obrigada à Super-mãe, Super-mulher e Super-tudo, que por mais difícil que a vida se encontrasse e por mais cansativos que os dias fossem, nunca desanimou nem baixou a cabeça. Digo-te uma e outra vez: quem me dera algum dia ser metade da mulher que és. Por último, aos meus dois irmãos, Rúben e Rafael, que conseguem ser ainda mais *nerds* que eu e que vão ser os meus melhores amigos para a vida. Rubito, o melhor *big brother* que alguém pode ter e que eu vou sempre admirar e ouvir atentamente. Rafinha, a pessoa mais parecida comigo à face da Terra, o meu *partner in crime* e o bebé da mana. Obrigada também às minhas cunhadas, Ana e Carolina, em quem eu gosto mais de pensar como nas irmãs que os meus irmãos escolheram para mim. Não me podia esquecer também da minha pe(canita) Gugui, que nunca falhou em fazer-me companhia.

Por último, obrigada ao David por todo o amor, carinho, paz, companheirismo e compreensão. Que todos os nossos planos a curto e a longo prazo se realizem, pois nós estamos cá para trabalhar e lutar por eles, juntos. Que as memórias do passado e a esperança no futuro nos continuem a unir no presente. Para sempre agradecida de te ter na minha vida. Obrigada também aos sogrinhos Dona Irina e Senhor João, ao Yuri e à minha sobrinha Maria Inês.

Abstract

Unraveling the functioning of the brain has been one of the greatest challenges of the scientific community. In order to obtain a full understanding of how neurons - the building blocks of the brain - coordinate their activity, tools capable of monitoring neural dynamics are necessary. It is possible to acquire neural data with high temporal and spatial resolution by placing flexible electrocorticography transparent electrodes over the brain surface, and measuring the electric potential variation while observing neurons activity with functional calcium imaging.

In this project, transparent and flexible microelectrode arrays made of patterned metal grids were produced using microfabrication techniques, namely maskless photolithography through direct laser writing, reactive ion etching, and electron beam evaporation of gold. Afterwards, the device was characterized in saline solution and also tested in mice cerebellum. It is here demonstrated that the electrocorticography device is easily reproducible. Patterned metal grids with 1 μm of linewidth and 22 μm of spacing showed an individual sheet resistance of 6 Ω/sq, and a transmittance of 80% at 550 nm. As for the device itself, the microelectrode array has 16 electrodes with 500 μm of diameter distributed over 3 mm. Additionally, an improved mechanical stability, through Parylene-C flexible substrate pre-treatment, and an impedance of 13 kΩ at 1 kHz were attained. *In vivo* tests also showed the microelectrode array efficiency for its primary goal: recording brain activity.

Hence, the presented microelectrode arrays are able to combine the superior temporal resolution of extracellular electrophysiology, offered by these low impedance electrocorticography electrodes, with the spatial resolution provided by functional calcium imaging in association with the transparent electrodes.

Keywords: Electrocorticography; Microelectrode Array; Patterned Metal Grids; Direct Laser Writing; Transparent and Flexible Electronics; Functional Calcium Imaging.

Resumo

Desvendar o funcionamento do cérebro tem sido um dos maiores desafios da comunidade científica. De modo a obter uma compreensão integral de como os neurónios – os principais constituintes do cérebro – coordenam a sua atividade, são necessárias ferramentas capazes de monitorizar a dinâmica neuronal. É possível adquirir dados neuronais com elevada resolução temporal e espacial, colocando elétrodos transparentes de electrocorticografia sobre a superfície cerebral, e medindo a variação do potencial elétrico enquanto se observa a atividade dos neurónios.

Neste projeto, matrizes de microeléctrodos transparentes e flexíveis, constituídas por redes de metal padronizadas, foram produzidas utilizando técnicas de microfabricação, designadamente fotolitografia sem máscara através de gravação direta a laser, erosão por iões reativos e deposição de ouro por evaporação assistida por canhão de eletrões. Posteriormente, o dispositivo foi caracterizado em solução salina e testado no cerebelo de ratos. É aqui demonstrado que o aparelho de electrocorticografia é facilmente reprodutível. As redes de metal padronizadas com 1 μm de largura de linha e 22 μm de espaçamento demonstraram uma resistência-folha individual de 6 Ω/sq e uma transmitância de 80% a 550 nm. Quanto ao dispositivo em si, a matriz tem 16 microeléctrodos de 500 μm de diâmetro cada distribuídos ao longo de 3 mm. Adicionalmente, foi obtida uma estabilidade mecânica melhorada, através de um pré-tratamento ao substrato flexível de Parileno-C, e uma impedância de 13 kΩ a 1 kHz. Os testes *in vivo* também demonstraram a eficácia dos elétrodos no seu objetivo principal: registar a atividade cerebral.

Deste modo, o dispositivo apresentado combina a elevada resolução temporal da eletrofisiologia extracelular, oferecida pelos elétrodos de electrocorticografia de baixa impedância, com a resolução espacial fornecida pela imagem funcional de cálcio em conjunto com os elétrodos transparentes.

Palavras-chave: Electrocorticografia; Matriz de Microeléctrodos; Redes de Metal Padronizadas; Gravação Direta a Laser; Eletrónica Transparente e Flexível; Imagem Funcional de Cálcio.

Contents

Acknowledgements i

Abstract iii

Resumo v

Contents........ vii

List of Figures........ xi

List of Tables xiii

List of Abbreviations and Acronyms........ xv

List of Symbols........ xvii

Motivation and Objectives 1

1. Introduction 3

  1.1 Electrocorticography 3

  1.2 The Electrical Properties of the Neurons........ 4

  1.3 Combining Electrophysiology with Optical Imaging........ 4

  1.4 Electrode Materials........ 5

    1.4.1 Metallic Nanostructures........ 6

    1.4.2 Patterned Metal Grids (PMGs) 7

2. Materials and Methods 9

  2.1 PMG Simulation and Design........ 9

  2.2 PMG Fabrication 9

  2.3 PMG Characterization........ 10

  2.4 ECoG Prototype Fabrication 10

  2.5 ECoG Prototype *In Vitro* Characterization........ 12

  2.6 *In Vivo* Characterization 12

3. Results and Discussion........ 13

  3.1 PMG Geometry Assessment........ 13

  3.2 Photoresist Resolution Study with DLW........ 13

  3.3 Patterning Gold PMGs 14

3.3.1 Control Mask Layout 14

3.3.2 Wet-Etching 15

3.3.3 Lift-off 16

3.4 PMG Linewidth 17

3.4.1 Optical Proximity Effect 17

3.4.2 Linewidth Study 18

3.5 PMG Characterization 18

3.5.1 PMG Simulation 18

3.5.2 Comparison of Simulation with Experimentation 19

3.5.3 Comparing PMGs with TCOs 21

3.5.4 Gold Structural Characterization 22

3.6 PMG Production on Parylene-C 22

3.6.1 Oxygen Dry Etching as a Pre-treatment 23

3.6.2 Bending Tests 26

3.7 ECoG MEA Production 27

3.8 ECoG MEA Characterization 28

3.8.1 *In Vitro* Characterization 28

3.8.2 *In Vivo* Characterization 30

3.8.3 Neural Data Analysis 31

4. Conclusions and Future Perspectives 33

References 35

Appendices 41

Appendix A – Overview of PMG materials, fabrication techniques, dimensions, and results for different geometries 41

Appendix B – Accessory used for transmittance measurements 45

Appendix C – Encapsulation Photolithography Mask Fabrication Process 46

Appendix D – Wet-etching Protocol and Setup 47

Appendix E – Profilometry measurement of E-Beam PVD of gold 48

Appendix F – Gold PMGs' SEM Images 49

Appendix G – Oxygen dry etching effect on gold color 50

Appendix H – Control Devices 51

Appendix I – Pictures taken during surgery 52

Appendix J – Other works related to the master thesis project 53

  Appendix J.1 53

  Appendix J.2 54

List of Figures

Figure 1.1 – Illustration of the major types of electrode interfaces of the brain……………………………...3

Figure 1.2 – Schematic of *in vivo* characterization of ECoG MEAs with simultaneous extracellular recordings and functional calcium imaging during mice walking……………………………………………………….5

Figure 1.3 – Schematic of the effects on electrical conductivity and optical transmittance by increasing the linewidth and pitch size of PMGs…………………………………………………………………...…7

Figure 1.4 – Schematic comparison of the performance/fabrication cost trade-off between some promising ITO-alternatives that are being explored for future transparent and flexible applications………………………7

Figure 1.5 – Optimization of transparent, conductive, biocompatible, and flexible PMGs……………………8

Figure 2.1 – ECoG MEAs fabrication schematic (not to scale)……………………………………………11

Figure 3.1 – Overview of the average transmittance and sheet resistance results of different PMG geometries, where the symbols in the light orange zone represent suitable options for the transparent electrodes…………13

Figure 3.2 – Control mask layout with different PMG dimensions and a gradient of linewidths…………….15

Figure 3.3 – Structures after wet etching 4-minute process observed under the optical microscope…………16

Figure 3.4 – Structures after lift-off method under the optical microscope…………………………………...16

Figure 3.5 – Comparison between linewidths…………………………………………………………...18

Figure 3.6 – Current density represented in false colors through COMSOL Multiphysics……………………19

Figure 3.7 – Schematic of the PMG simulation structure on Ansys Lumerical - FDTD Solver………………19

Figure 3.8 – Simulational and experimental results comparison……………………………………..……21

Figure 3.9 – Transmittance spectra of the IZO sample (200 nm thick) and of the selected gold PMG, with the visible range denoted………………………….………………………………………………………22

Figure 3.10 – Structural analysis of the gold used in PMG fabrication…….………………………………22

Figure 3.11 – Different times of oxygen dry etching pre-treatment effect on the sheet resistance of a 80 nm thin film of gold………………………………………………………………………………………….24

Figure 3.12 – Effect of oxygen dry-etching in the linewidth of PR patterned structures………………………25

Figure 3.13 – Effect of oxygen dry etching pre-treatment on PMG on Parylene-C……………..…………….26

Figure 3.14 – Testing sheet resistance variation of gold PMG during bending cycles………………………...26

Figure 3.15 – Prototype with 16 gold PMG electrodes…………………………………………………….…27

Figure 3.16 – Transparent and flexible ECoG MEA prototype……………………………………………….27

Figure 3.17 – Impedance magnitude measured at 1 kHz in saline solution……………………………………28

Figure 3.18 – Pictures from implantation surgery……………………………………………………………30

Figure 3.19 – Mouse positioned on the behaviour and imaging setup with the device implanted in its cerebellum………………………………………………………………………………………………......30

Figure 3.20 – Neural data acquired during mouse walking on treadmill at the time of movement trigger…......31

Figure B.1 – A) Accessory for transmittance measurements; B) Schematic of PMG design with the four contacts for Hall measurements (each contact has 1 mm on the side), and with the limited circular area for transmittance analysis (2 mm of diameter), having the whole design in total 3 mm^2……………….……….45

Figure C.1 – Encapsulation mask designed in KLayout……………………………………………………46

Figure D.1 – Gold wet etching setup……………………………………………………………………47

Figure E.1 – Measured Ti/Au thickness in the different quadrants of the E-Beam substrate holder platform……………………………………………………………………………………………48

Figure F.1 – SEM images of the gold PMGs……………………………………………..………………...49

Figure G.1 – ECoG prototypes and PMGs with gold color affected by the oxygen dry etching pre-treatment…………………………………………………………………………………………....50

Figure H.1 – Control devices…………………………………………………………………………51

Figure I.1 – ECoG prototype assembled with the ZIF adapter……………………………………………..52

Figure I.2 – Mouse in its cage already with the headbar and cranial window…………………………………52

List of Tables

Table 1 – Positive and negative photoresist patterns with different dimensions analyzed with SEM……..…14

Table 2 – Wet-etching effect on a sample over 4 minutes…………..………………...………………………..15

Table 3 – Proximity effect analysis in positive photoresist patterned grid and gold PMG…………..………..17

Table 4 – Optical and electrical PMGs characterization obtained through experimentation, considering a decrease in linewidth, with a constant spacing of 10 µm…………………………...18

Table 5 – Optical and electrical PMGs characterization obtained through experimentation and through simulation, considering an increase in spacing (from 6 µm to 22 µm, with a constant linewidth of 1 µm)….…20

Table 6 – Atomic force microscope scans showing oxygen plasma pre-treatment effects on Parylene-C and gold surface roughness…………………………………………………………………………………..23

Table 7 – Gold thin film sheet resistance values on different conditions……………………………………...25

Table 8 – Impedance results for the final prototype and for the control prototype……………………..……...28

Table 9 – Current transparent electrodes and their dimensions, impedance magnitude at 1 kHz in saline solution, sheet resistance and transmittance value at 550 nm..…………………………………..……………29

Table A.1 – Square PMG……………………………………………...…………………………………...41

Table A.2 – Rectangular PMG……….…………………………………………………………………….42

Table A.3 – Circular PMG………………..………………………………………………………………..43

Table A.4 – Honeycomb PMG………………………...…………………………………………………...44

Table A.5 – Triangular PMG……………….………………………………………………………………44

Table A.6 – Asymmetric PMG (pentagonal)………...……………………………………………………..44

List of Abbreviations and Acronyms

AC	Alternating Current
AFM	Atomic Force Microscopy
AP	Action Potential
BCI	Brain-Computer Interface
CaM	Calmodulin
CEMOP	Centro de Excelência de Optoeletrónica e Microeletrónica de Processos
CENIMAT	Centro de Investigação de Materiais
CNT	Carbon Nanotube
CVD	Chemical Vapor Deposition
DC	Direct Current
DCM	Departamento de Ciência dos Materiais
DI-Water	Deionized Water
DLW	Direct Laser Writing
E-Beam	Electron Beam Evaporation System
ECoG	Electrocorticography
EEG	Electroencephalography
EIS	Electrochemical Impedance Spectroscopy
EMG	Electromyography
FCT – NOVA	Faculdade de Ciências e Tecnologia da Universidade Nova de Lisboa
FDTD	Finite Difference Time Domain
FEM	Finite Element Method
FOM	Figure of Merit
GCaMP	GFP fused with CaM
GDS	Graphic Design System
GFP	Green Fluorescent Protein

GND	Ground
i3N	Instituto de Nanoestruturas, Nanomodelação e Nanofabricação
IPA	Isopropyl Alcohol
ITO	Indium Tin Oxide
IZO	Indium Zinc Oxide
LFP	Local Field Potential
MEA	Micro-Electrode Array
MUA	Multi-Unit Activity
NA	Not Available
NIR Light	Near Infrared Light
NW	Nanowire
PEDOT	Poly-3,4-ethylenedioxythiophene
PMG	Patterned Metal Grid
PPy	Polypyrrole
PR	Photoresist
PVA	Polyvinyl Alcohol
PVD	Physical Vapor Deposition
RF	Radiofrequency
RIE	Reactive Ion Etching
RMS	Root Mean Square
SEM	Scanning Electron Microscopy
SNR	Signal-to-Noise Ratio
TCE	Transparent Conductive Electrode
TCO	Transparent Conductive Oxide
UV Light	Ultraviolet Light
Vis Light	Visible Light
XRD	X-Ray Diffraction
ZIF	Zero Insertion Force

List of Symbols

G	Gain
g	Gram
h	Thickness
I	Electric Current
J	Current Density
m	Meter
ºC	Celsius Degrees
P	Power
p	Pitch
rpm	Revolutions per Minute
s	Seconds
sccm	Standard Cubic Centimeter per Minute
T (%)	Transmittance
V	Voltage
w	Width
wt. %	Weight Percentage
Z	Impedance
R	Electrical Resistance
Ω/sq	Sheet-Resistance

Motivation and Objectives

The main purpose of this project is to fabricate transparent electrocorticography (ECoG) Microelectrode Arrays (MEAs). Brain activity generates electrical signals that we can detect using an electrode made of a conducting material. ECoG is an electrophysiological monitoring tool that uses MEAs placed in the brain surface to detect electrical signals generated from neural activity. A full understanding of how neurons coordinate their activity to elegantly produce behavior in animals will require devices capable of sensing neural signals across multiple brain regions, ideally with the extra ability to simultaneously distinguish different types of neurons, as well as their exact location, which can be attained through optical imaging [1]. Functional calcium imaging is a microscopy technique where the activity of genetically-identified neurons can be detected optically using fluorescent calcium-sensitive dyes or proteins into the cell membranes of neurons [2]. However, these calcium signals are relatively slow and cannot give precise information about the timing of neural activity relative to animal behavior. In this way, functional calcium imaging associated with transparent MEAs can be used to obtain the necessary temporal resolution given by the MEAs used to measure the neural activity with sub-millisecond precision. This device can cover a wide area of the brain surface, without penetrating the brain, measuring the dynamics of many neuron populations, thus providing a view of large-scale neural activity. For these reasons, the motivation for this work comes from the need to produce and test transparent ECoG MEAs.

Primarily, it is desired that the device is flexible, so it can adapt to the curvilinear surface of the brain. In addition, the electrodes need to be transparent in order to be used alongside functional calcium imaging, but they also need to be as conductive as possible. In such manner, there is an interplay between the resistivity of the chosen electrode material and its transmittance. Nowadays, in the field of transparent and flexible electronics, new materials and structures are being studied. There have been promising attempts to build transparent MEAs using Indium-Tin Oxide (ITO) [3] and graphene [4], [5]. However, they were not widely adopted by neuroscientists. While graphene presents remarkable properties, its fabrication by reproducible and large-scale methods is still very challenging. Regarding ITO, due to indium scarcity and brittleness, a number of alternatives are currently under active research. Thus, Patterned Metal Grids (PMGs) are currently considered one of the best candidates due to their high electrical conductivity, optical transparency, mechanical robustness, and cost competitiveness [6]. Moreover, it is possible to optimize PMGs and MEAs dimensions down to the sub-micron scale by using state-of-the-art techniques such as Direct Laser Writing (DLW) [7]. Lastly, considering that the PMG material must be biocompatible, stable under physiological conditions, highly conductive, and somewhat flexible, gold appears to be a suitable option.

Therefore, this project aims to study and optimize, and then embed, gold PMGs in the electrodes so they can be highly efficient, transparent, and conductive, providing both spatial and temporal resolution, with the ultimate goal of improving neural data acquisition.

In order to achieve the main objective, the following tasks will be performed:

- Simulations on the PMG electrical and optical properties to explore the effect of PMG dimensions, in COMSOL Multiphysics® software and Ansys Lumerical – FDTD (Finite-Difference Time-Domain) Solver, respectively;
- Design the PMGs in KLayout considering the results offered by simulations;
- Manufacture of the PMGs using microfabrication techniques such as high-resolution photolithography equipment (DLW), gold Physical Vapor Deposition (PVD), and lift-off patterning, whilst optimizing the protocol;
- Electro-optical characterization of the PMGs and selection of the one with the best performance;
- Design of the ECoG device itself, incorporating the chosen PMG in the electrodes;
- ECoG device production and wrap up of the protocol optimization;
- ECoG electrochemical and morphological characterization;
- *In vivo* characterization and proof of concept.

This work received funding from the European Community's H2020 program under grant agreement no. 716510 (ERC-2016-STG TREND) and no. 952169 (SYNERGY).

1. Introduction

1.1 Electrocorticography

In order to better understand the brain and its associated diseases it is necessary to encourage new studies concerning the data acquisition from neural activity. In this context, the electrocorticography (ECoG), also known as intracranial electroencephalography (iEEG), is an electrophysiological monitoring tool capable of recording neural signals. Clinical applications on this matter include the tracking of epileptogenic zones and the advancement of therapies and rehabilitation solutions in neurological disabled patients. Moreover, the growing interest in connecting the human brain with machines has led to the development of a wide range of neural devices. Even the technology leading enterprises, Facebook (Reality Labs) [8] and Neuralink (led by Elon Musk) [9], are starting to recognize the impact that brain-computer interfaces (BCIs) can have in the near future. However, Neuralink's device is extremely invasive, since the microelectrodes implantation (**Figure 1.1**) damages the blood-brain barrier [10], [11] which triggers an acute immune response followed by a chronic inflammation and neural degeneration around the implant, that can dramatically impact the readout of electrical signals, and ultimately lead to device failure [12]. Here, we expect to produce ECoG microelectrode arrays (MEAs) on a flexible and ultrathin polymeric substrate which is then laid on the surface of the cerebellar cortex, measuring the activity of multiple neurons simultaneously, providing a view of large-scale activity. Despite of ECoG's invasive nature and the need to have a craniotomy, it is not as invasive as the penetrating electrodes as shown in **Figure 1.1**. Additionally, when compared to the EEG, ECoG allows to measure local field potentials (LFPs) with increased quality since the ECoG is placed below the skull, which presents a low electrical conductivity [13]. As a result, the ECoG will have a higher spatial resolution than the EEG, as well as higher amplitude, higher signal-to-noise ratio (SNR), and it is not susceptible to artifacts such as electromyographic (EMG) signals [14]–[16]. Moreover, recently, high-density MEAs with small electrodes have allowed to record individual action potentials (APs) of neurons, multi-unit activity (MUA) and microscopic LFPs [17]–[20]. Therefore, we can conclude that in order to obtain optimal neural recordings, it is somehow necessary to overcome the bone barrier, but it is also essential to keep the integrity of the brain by analyzing neural populations without damaging any tissue.

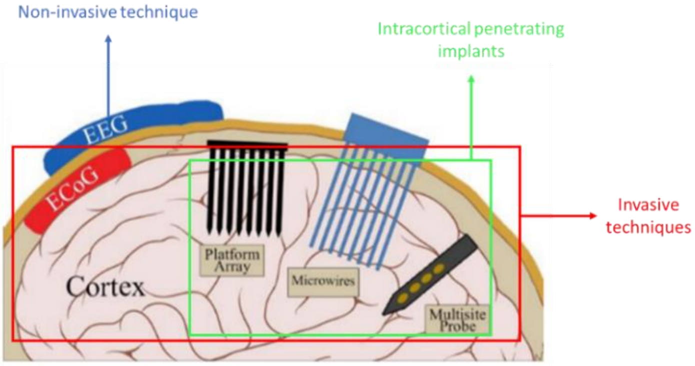

Figure 1.1 – Illustration of the major types of electrode interfaces of the brain. The EEG is the only non-invasive neuronal recording technique displayed. The platform array, as well as the microwires and multisite probe, are implanted through the penetration of the brain tissue. The ECoG seems the best trade-off between non-invasive tools (that do not offer a fine temporal resolution) and intracranial electrodes (that provide excellent recordings but trigger an intense immune response). [Adapted from [20]]

1.2 The Electrical Properties of the Neurons

Neurons are the building blocks of the brain, and the brain has billions of them. The neurons are intertwined in a complex way, communicating with each other through synapses, processing information within milliseconds. Neural activity is mediated by the flow of ions across the neuronal membrane, both into and out of the cell. These currents, whether at synaptic sites or during APs, can be measured as changes in the electric potential at a point in the extracellular space, compared to a reference point. APs are the fundamental unit of signaling in the nervous system, and consist in a fast variation of 1 kHz in the range of tens to hundreds of microvolts in amplitude. LFPs, slower frequencies (< 300 Hz) in extracellular recordings, are thought to reflect synchronized synaptic currents, as these occur over slower timescales (tens of milliseconds), so there is more opportunity for signals from multiple cells to summate and result in larger signals (range from hundreds to thousands of microvolts). Although there are many kinds of neurons, the same basic electrical principles underlie their function. In the present study, we will measure the electrical signals from putative Purkinje cells populations, which are located in the cerebellum and exhibit an elaborate dendritic arbor [21]–[23].

1.3 Combining Electrophysiology with Optical Imaging

ECoG is a form of extracellular recording whose signals are often composed by LFPs [20]. In one hand, ECoG can provide a temporal resolution on the millisecond scale. On the other hand, each electrode is sensitive to the activity of hundreds of neurons in its vicinity and to all transmembrane currents in the extracellular space (*e.g.*, synaptic and AP currents). Thus, the recorded signal cannot reveal exact locations of active neurons, and can only provide cell-type information if used in combination with photostimulation. Due to the uncertainty regarding the precise neural generator of the LFP [24], the addition of a tool capable of providing the intended spatial resolution will be beneficial. It is possible to increase spatial resolution in order to associate which neuron population is generating the recorded LFP, and consequently animal behavior, by associating ECoG with optical imaging [25]. With functional calcium imaging, we can measure calcium signaling using fluorescent indicators such as GCaMP (Green Fluorescent Protein (GFP) fused with calmodulin (CaM)). Neurons with fluorescent indicators for calcium – GCaMP – are excited by a light source and, in turn, emit light. When a neuron is active, GCaMP will emit more light due to calcium influx [26]–[28]. Therefore, fluorescence operates as a representation of neural activity. In such manner, using functional calcium imaging will provide us with the spatial resolution that the ECoG measurements alone do not possess, while ECoG recordings will contribute with temporal resolution that the functional calcium imaging does not offer. Consequently, we expect to obtain high spatio-temporal resolution outcomes by combining these techniques, which is possible by developing transparent ECoG MEAs in order to monitor fast and large-scale neuronal activity [29].

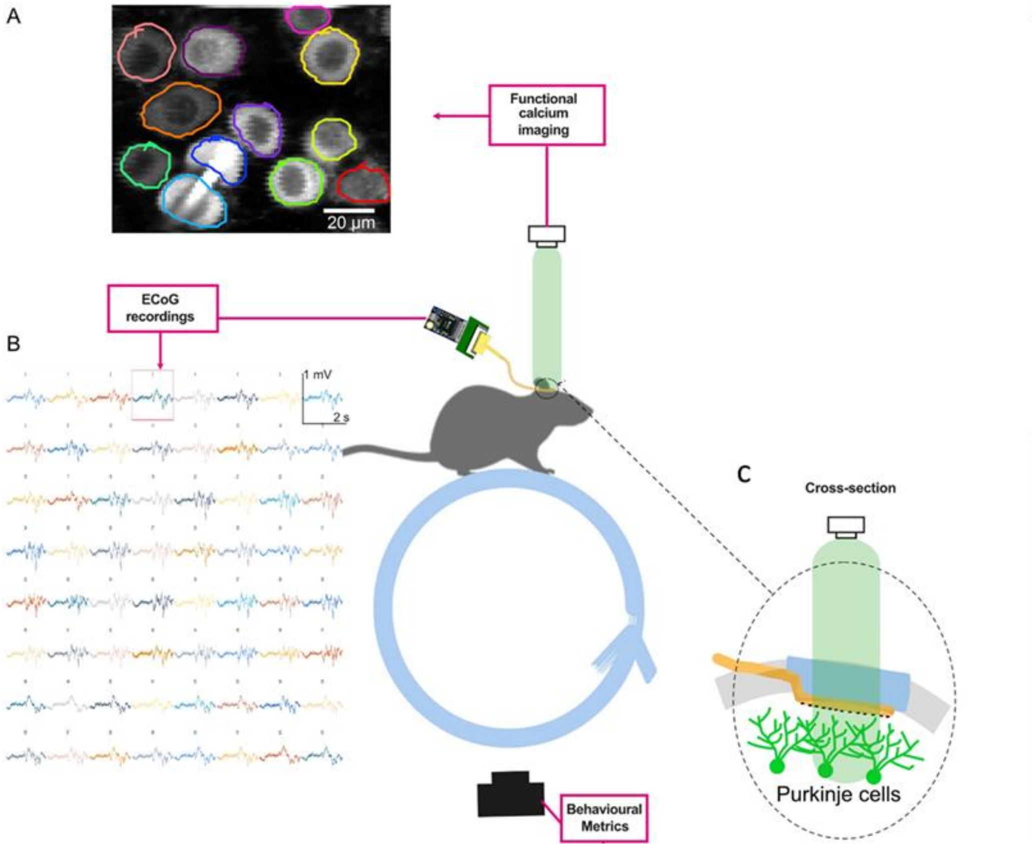

Figure 1.2 – Schematic of *in vivo* characterization of ECoG MEAs with simultaneous extracellular recordings and functional calcium imaging during mice walking. A) An example of two-photon imaging of Purkinje cells [30]; B) An example of ECoG recordings obtained from the cerebellar cortex. C) Cross-sections of a 3 mm cranial window showing simultaneous ECoG and imaging recordings from Purkinje cells. [Adapted from [31]]

1.4 Electrode Materials

Regarding the materials for the flexible and transparent ECoG MEAs, these must be chosen taking into consideration the application. For instance, being transparent is one of the most relevant characteristics since the goal is to observe the activity of fluorescent neurons with the functional calcium imaging technique through the electrode. Furthermore, the electrode material requires other significant properties, namely being a biocompatible material, having good and stable electro-optical characteristics, as well as an appropriate mechanical robustness [32]. This last parameter is also one of the most important because it influences the device stability and performance, since the device will have to adapt to non-uniform and curvilinear surfaces, such as the cerebral cortex or the cerebellum. As a result, the device substrate must be thin, conformable, transparent, and inert, being Parylene-C a common choice for these applications [33].

When it comes to electrode material itself, many materials, not originally developed for neural interfaces but for optoelectronic applications, become promising candidates to detect neural signals [34]. There have been interesting attempts to build transparent ECoG electrodes using metal [33], [35]–[38], transparent conductive oxides (TCOs) [3], [39], [40], graphene [5], [41], and conductive polymers [42]–[44]. TCOs are an interesting class of materials which exhibit a significant combination of high electrical conductivity and optical transparency [45]. For neural interfaces, two types of TCOs are commonly used: ITO and indium zinc oxide (IZO). However, ITO and IZO present some drawbacks such as their ceramic brittle nature being inappropriate for flexible electronics [6] and indium high cost. Additionally, for *in vivo* applications with infrared light, ITO oxidizes over time, resulting in a change of optical properties of the film, influencing biocompatibility properties, and increasing electrical impedance [46]. The prominent graphene has also been used in ECoG electrodes for being highly conductive, ultra-thin, transparent, and mechanically resistant. Nevertheless, its fabrication by reproducible and large-scale methods is still challenging. Although some studies showed that graphene electrodes can be artefact-free, under some conditions it may induce photoelectric artefacts and contaminate neural data [46]. There is also another carbon-based material displaying this problem: carbon nanotubes (CNTs). Despite its good mechanical, optical and electrical properties, exceptional flexibility and proper work function [47], CNTs do not possess a suitable purity, and normally contain a mixture of several materials including catalyst particles, and amorphous or non-tubular carbon. Moreover, CNTs for biomedical applications need to be evaluated due to its potential toxicity [48]. Another group used in transparent conductive electrodes (TCEs) are conductive polymers, such as polypyrrole (PPy), and poly-3,4-ethylenedioxythiophene (PEDOT) [44]. Although polymers present some interesting features for flexible electronics applications, one of the main problems for its usage is their electrical stability over time, since electrical conductivity decreases when the mentioned polymers are exposed to high temperatures, humidity or ultraviolet (UV) light [49]. Nevertheless, conductive polymers are largely adopted for electrode coatings due to their biocompatibility [50]. In addition, incorporation of biomolecules in these polymers appears to be beneficial in increasing cell interactions with the electrodes' surface [51].

1.4.1 Metallic Nanostructures

Metals are amongst the most conductive materials due to their typical high free-electron density. However, in order for them to be transparent, they may adopt different configurations, such as ultrathin film structures, nanowire (NW) networks, or patterned into a metal grid (PMG) [49]. Both NWs networks and PMGs are in a sense analogous since they possess optically transparent holes. Typically, AgNWs are widely used due to the intrinsic high conductivity of silver [52]. However, electrical stability utilizing this type of nanostructure is a concern in the long run, as silver can oxidize [53]. There is a wide range of metals that can be used due to their biocompatibility for neural devices, being gold (Au), silver (Ag), and platinum (Pt) some examples. Some studies comparing these metals have been carried out, showing that Au performs better than Ag and Pt [6]. Gold appears to be a suitable option due to its biocompatibility, its high work function (which makes it oxidation and corrosion resistant) and its ductility [36].

A survey regarding the materials used in transparent electrodes for neural applications can be seen later in **Table 9**.

1.4.2 Patterned Metal Grids (PMGs)

In this project, we aim to produce PMGs because of the advantages it offers. When compared to a continuous metal film, the area between the grid lines is absent of material, causing an increase in the PMGs transmittance values [37]. However, since there is less material for conduction electrons to flow, there is also an increase in sheet resistance. Therefore, an interplay between these two parameters must be achieved. Grid dimensions can be manipulated down to the sub-micrometer scale [54]. The control and resolution of grid design some fabrication techniques offer, such as direct laser writing, are essential to guarantee certain electro-optical properties. For example, by optimizing linewidth and pitch (spacing plus linewidth), it is possible to adjust electrical conductivity and optical transmittance to optimal values, as shown in **Figure 1.3**.

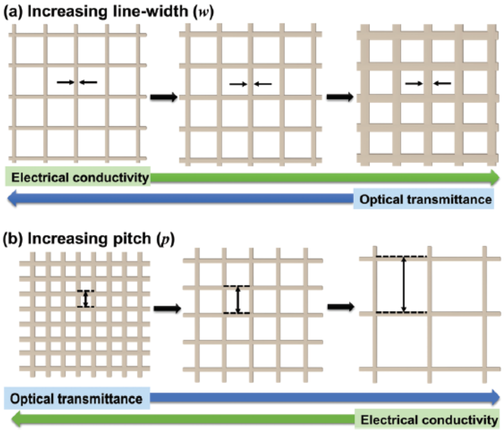

Figure 1.3 – Schematic of the effects on electrical conductivity and optical transmittance by increasing the (a) linewidth and (b) pitch size of PMGs [6].

PMGs can be used for applications where surface roughness is not an issue, such as extracellular electrodes, since the roughness is desirable as it increases the electrode surface area and electrode capacitance, and decreases impedance magnitude. In conclusion, PMGs are considered to be one of the best candidates due to their high electrical conductivity, optical transparency, mechanical robustness, and cost-competitiveness (as shown in **Figure 1.4**) [6].

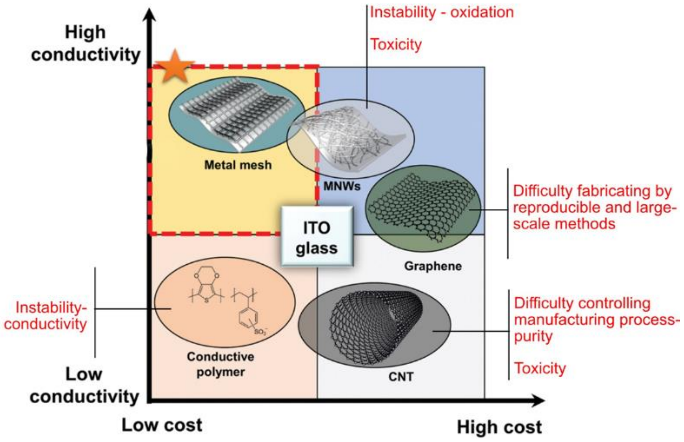

Figure 1.4 – Schematic comparison of the performance/fabrication cost trade-off between some promising ITO-alternatives that are being explored for future transparent and flexible applications, including metal NWs, PMGs, conductive polymers, CNTs and graphene. The drawbacks of CNTs, graphene, MNWs and conductive polymers are listed next to each material. PMGs are suggested as the best candidates. [Adapted from [6]]

Through the design of grid dimensions, new geometries of the metal network can be created. These include square grids [55], honeycomb structures [56], and circular shapes [36], [57]–[59]. Other structures have been studied, being these last three the most commonly produced (**Appendix A**). The PMGs with the highest percentage of metal area coverage are also the PMGs with the lowest sheet resistance. Contrarily, the PMGs with the lowest percentage of metal area coverage are the ones with the highest transparency values [60]. Additionally, since the project aims to produce state-of-the-art MEAs, the technique precision is of extreme importance. Therefore, DLW is a very suitable option for PMG manufacture. The theoretically maximum resolution of the equipment we are going to use is 600 nm, so we can exploit linewidth resolutions down to 600 nm [7].

In **Figure 1.5**, the geometric parameters used in the study are detailed. Additionally, some examples of devices produced in Parylene-C are shown. Parylene-C will be the substate in which the ECoG device will be built in.

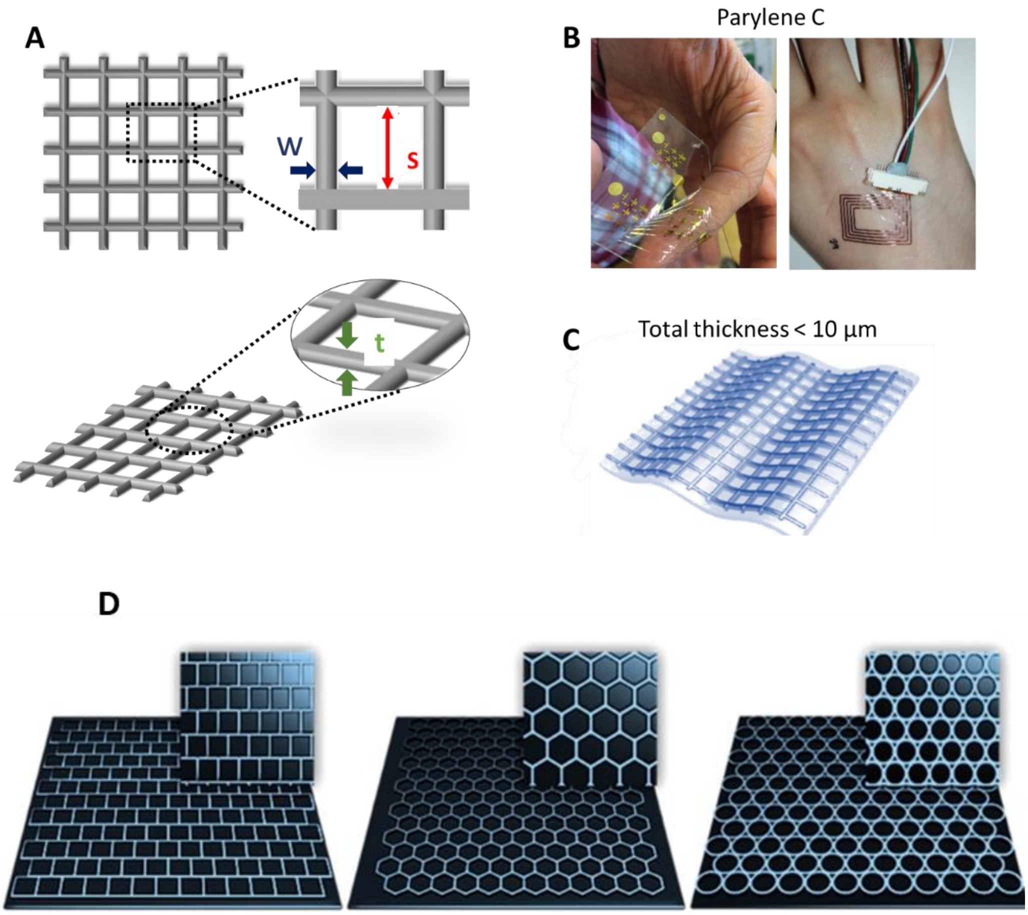

Figure 1.5 – Optimization of transparent, conductive, biocompatible, and flexible PMGs. A) The effect of PMG dimensions, such as the spacing (s), the line width (w), and its thickness (t), will be evaluated on the electro-optical properties of PMGs. B) Prototypes built in Parylene-C substrates within the research group. C) The MEAs with the embedded PMGs will be fabricated on transparent and flexible membranes of Parylene-C. D) Area coverage of different metal grid geometries with 5 µm linewidth: square grids (19% metal area coverage), honeycomb structures (22% metal area coverage), and circular shapes (47% metal area coverage) [6].

2. Materials and Methods

The content in this chapter summarizes the simulation, design, production, and characterization processes used to obtain and test both the PMGs and the final ECoG device.

2.1 PMG Simulation and Design

In order to assess the effect of PMG dimensions on their electrical and optical properties, simulations were made using COMSOL Multiphysics® software (AC/DC module) and Ansys Lumerical – FDTD Solver, respectively. COMSOL simulations, based on a previous work from our team [61], provided a better insight on the electrical properties of the PMGs by numerically modeling them via FEM (Finite Element Method). A potential of 1 V was applied across the simulated PMG and the current density, J (A/m^2), was calculated. Lastly, sheet resistance values were also taken from simulations. A gold thickness of 80 nm was kept during all simulations, as well as a linewidth of 1 µm, only varying the spacing between lines. The glass substrate and titanium adhesion layer were not considered on behalf of simulation time. Optical FDTD simulations were carried out using Lumerical software to assess the transmittance of each PMG. Since PMG structure is periodic, the FDTD region was reduced to only one period (one square) to reduce simulation time. In these simulations, glass was considered since the transmittance monitor is behind the glass substrate and it influences transmittance values. Even though real glass thickness is approximately 1 mm, a 600 nm thick glass was considered to reduce processing time as well. Regarding PMG design for fabrication, it was achieved by using KLayout software and stored in GDS (Graphic Design System) format. These designs are in separate files so that it is possible to produce them individually due to each PMG line density. Each of the PMG differentiates only in spacing sizes (from 6 µm to 22 µm), according to the results previously obtained in the simulations, and have a Van der Pauw square structure for electrical characterization.

2.2 PMG Fabrication

The initial step was to properly clean several 2 x 2 cm glass substrates by first immersing them in acetone bath under ultrasounds for 10 minutes, followed by an IPA (isopropanol) bath also under ultrasounds for 10 minutes. The substrates were then rinsed with deionized water (DI-water) and blow dried with a nitrogen spray gun. Afterwards, each glass was spin-coated with positive photoresist (PR) AZ® ECI 3012, from MicroChemicals GmbH, for 10 s at 3000 rpm, then 20 s 4000 rpm, followed by a soft-bake at 110 ºC for 1 min. A DLW equipment, tabletop µPattern Generator 101 Heidelberg Instruments, was used to pattern the PMGs onto the positive PR, and the exposure conditions used were 15 mW at 40 % with filter, unidirectional approach, using writing mode I (2 µm head). This step was followed by a 30 s post exposure bake at 110 ºC, letting the sample cool down, then immersing it in developer solution (AZ® 726 MIF - MicroChemicals GmbH) and rinsed twice in DI-water, then blow dried with N_2 and hard-baked for 30 s at 110 ºC. Afterwards, a titanium-gold (± 6 nm and ± 80 nm of thickness, respectively) deposition was carried out by electron-beam evaporation, with an equipment built in-house. The deposition conditions used were 5.5×10^{-6} mbar for the initial chamber pressure, the applied current was 0.05 – 0.06 A, resulting in an average deposition rate of 0.8 nm/s at room temperature. The metal was later patterned by acetone lift-off, with the support of a soft brush, until Ti/Au layers were removed from the undesired places. Additionally, a parallel study on gold wet etching was made, whose protocol can be consulted in **Appendix D**.

2.3 PMG Characterization

PMGs' electrical characterization was performed in Nanometrics HL5500 Hall Effect Measurement Systems, with a 0.5 T permanent magnet, through the Van der Pauw Method in order to obtain sheet resistance values. Optical characterization took place in Spectrometer UV-Vis-NIR – Perkin Elmer Lambda 950 for transmittance measurements, using an integrating sphere, in the wavelength range from 250 to 1500 nm with a step of 5 nm and a gain of 2. The fabricated accessory used to measure the transmittance is depicted in **Appendix B**. It is also noteworthy that throughout the whole PMG fabrication process, the samples were constantly being analyzed using optical microscopy (Zeiss Axioscope 5 Optical Microscope), and some additional images were attained through Scanning Electron Microscopy (SEM, Zeiss Auriga Crossbeam Microscope).

2.4 ECoG Prototype Fabrication

The ECoG MEA was also designed in KLayout, as aforementioned for the PMGs. The substrates for the prototype (3-inch p-type silicon wafers) were cleansed in the same manner as the PMGs' glass substrates. Polyvinyl-alcohol (PVA) solution was used as a sacrificial water-soluble layer. It was prepared by dissolving 5 g of PVA solute (88 % hydrolyzed, average M.W. 20,000-30,000, Acros Organics) in 100 ml of DI-water (5 wt. %) in a glass flask with a magnetic stirrer (1000 rpm) heated at 90 ºC during a continued period of time. PVA solution was abundantly spread in the previously washed substrates using a syringe with a particle filter attached. The spinning conditions were 10 s at 3000 rpm, then 20 s at 4000 rpm, followed by 2 min at 110 ºC on the hot plate. Parylene-C deposition followed, and it was accomplished through a chemical vapor deposition (CVD) process using a Parylene Deposition System 2010 Labcoter^{TM} 2 by Specialty Coating Systems. A mass of 8.6 g of Parylene-C dimer was placed in the vaporizer in order to get a film thickness of approximately 5 μm. Temperature values used for Parylene-C deposition in different stages of the process were: 175 ºC for the vaporizer, 690 ºC in the pyrolysis chamber and 25 ºC in the deposition chamber. Then, PR patterning using the DLW equipment occurred likewise for the PMGs. Afterwards, an oxygen plasma pre-treatment was applied to the sample using Minilock – Phantom RIE (Reactive Ion Etching) from Trion Technology according to the conditions of 50 W of RF (radiofrequency) power, 10 sccm of flux, 50 mTorr of pressure, 25 ºC of temperature, and 300 s of duration. The next step was the titanium-gold deposition done in the same conditions as in the PMGs mentioned above. Ultrasonic lift-off using acetone was made for approximately 30 s, then placed in an IPA bath and finally rinsed with DI-water and dried with a nitrogen spray gun. For the encapsulation of the device, another Parylene-C deposition was carried, this time using only 2 g, which results in a theoretical thickness of 1 µm. Subsequently, in order to etch the previously deposited Parylene-C from the unwanted areas, such as the electrodes and the contact pads, a negative photoresist AZ® nlof 2020 from MicroChemicals GmbH was spin-coated during 30 s at 3000 rpm, and soft-baked at 110 ºC for 2 min. This photolithography process was made using a Karl-Suss MA6 UV Mask Aligner with an exposure time of 8 s, without filter, using a molybdenum mask shown in **Appendix C**. After the post-exposure bake at 110 ºC for 2 min, the sample was then developed as mentioned above for the PMGs, as well as for the MEA. Parylene-C etching took place in the RIE equipment using once more O_2 plasma, with the same conditions as before, but now for 1000 s. The sample was slightly washed in acetone and IPA, rinsed with DI-water, and dried with nitrogen spray gun. Finally, for the peel-off process, a recipient with DI-water at 90 ºC was used for immersing the prototype, whose edges had been previously scratched out. The Parylene-C membrane started to detach from the substrate, and it was then cleansed with DI-water and dried with N_2.

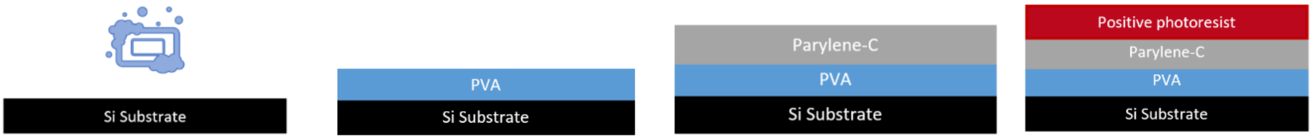

1. Substrate cleaning with acetone and IPA

2. PVA deposition

3. Parylene-C deposition

4. Positive PR deposition

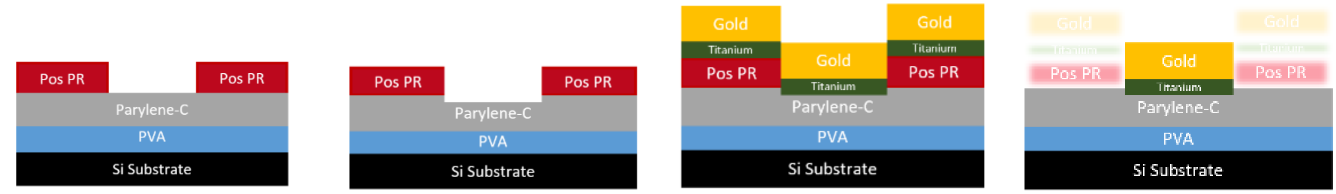

5. Exposure and posterior development

6. Oxygen plasma pre-treatment

7. Ti/Au deposition

8. Ultrasonic lift-off

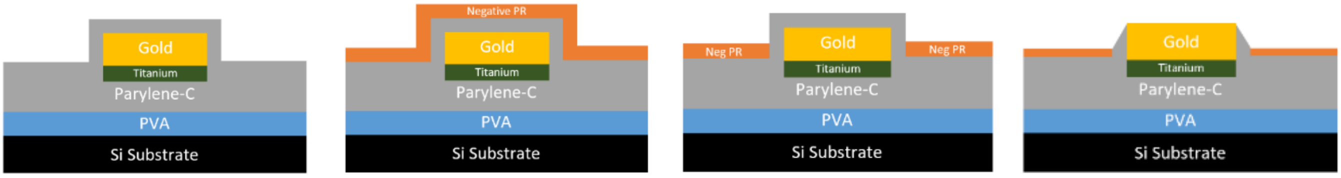

9. Parylene-C deposition

10. Negative PR deposition

11. Exposure and development

12. Parylene-C O_2 dry etching

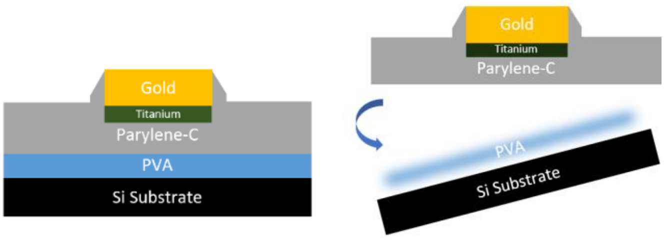

13. Cleaning

14. Peel-off

Figure 2.1 – ECoG MEAs fabrication schematic (not to scale). The last images (10 to 14) represent only the PMG in the electrodes and the contact pads, since the metallic vias are encapsulated with Parylene-C. Therefore, the cross-section schematic for the metallic vias stop at step number 9.

2.5 ECoG Prototype *In Vitro* Characterization

Throughout the microfabrication process of the ECoG device, the prototype was constantly analyzed by optical microscopy in order to guarantee the quality of the final prototype. Prototypes were then characterized by connecting them to an adapter equipped with a Zero Insertion Force (ZIF) and Omnetics connector, compatible with the measuring equipment, which comprises the Open Ephys acquisition board along with the RHD2000 series interface chip that amplifies and digitally multiplexes the signal from the 16 extracellular electrodes (Intan Technologies). The impedance magnitude at 1 kHz of each electrode was measured using a protocol implemented by the RHD2000 series chip from Intan, with a two-electrode cell configuration: the electrodes of the ECoG device and the reference electrode, an Ag/AgCl wire (Science Products GmbH, E-255), were immersed in saline solution and the contact pads connected to the ZIF adapter; the reference electrode was also immersed in saline solution.

2.6 *In Vivo* Characterization

After *in vitro* validation, *in vivo* characterization was performed beginning with the selection of the ECoG MEAs with better performance and higher yield (higher number of electrodes fully functional). The surgery consisted of the implantation of a headbar restraint on the skull and by a craniotomy in the anesthetized animal. The MEAs were laid on the surface of the cerebellum and covered with a glass window, which was then sealed on the skull with cyanoacrylate.

Then, during the surgery, we aimed to test the conformal contact of MEAs with exposed brain surface, evaluate implantation feasibility and compatibility with imaging and behavior setup, and troubleshoot extracellular recordings (*e.g.*, noise). Brain signals were recorded from the MEAs. Extracellular signals in a frequency band of 0.1 – 7500 Hz were sampled at 30 kHz with 16-bit resolution and were saved in a raw binary format for subsequent offline analysis using Bonsai interface. Finally, this acquired neural data was analyzed using code previously used in other works [62].

3. Results and Discussion

In this chapter, the results of the current work will be presented and discussed, according to the main goal of the project. This study focuses on the optimization and development of transparent and flexible ECoG MEA devices with gold PMGs embedded, followed by a careful characterization. The ulterior purpose is to use this prototype to study cerebellar activity with high spatial and temporal resolution.

3.1 PMG Geometry Assessment

Several PMG geometries have been produced not only for neural devices but mainly for optoelectronic applications, as aforementioned in Chapter 1. A literature overview regarding the transmittance and the sheet resistance of the different geometries was made, and the scrutinized results are contemplated in **Appendix A**. By averaging the values surveyed in literature, **Figure 3.1** was plotted. The light orange zone is where high values of transmittance (from 80% upwards) and low values of sheet resistance (< 20 Ω/sq) are represented. We can observe that square PMGs are within this region and that honeycomb PMGs are on the borderline. Therefore, the square geometry was adopted for this work due to its performance.

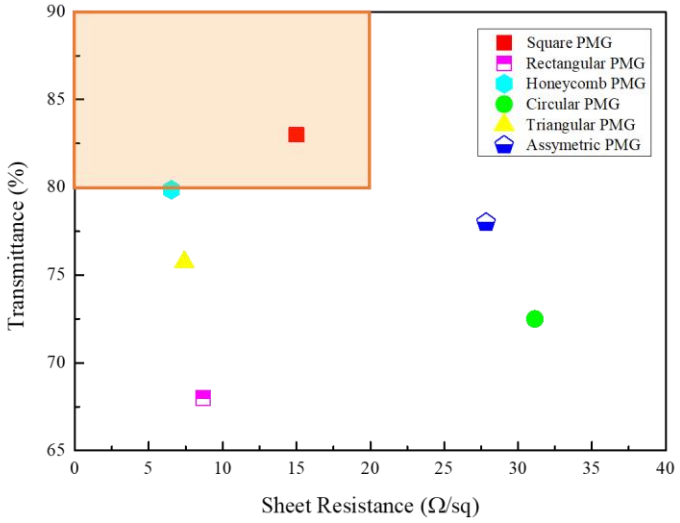

Figure 3.1 – Overview of the average transmittance and sheet resistance results of different PMG geometries, where the symbols in the light orange zone represent suitable options for the transparent electrodes.

3.2 Photoresist Resolution Study with DLW

In order to optimize the PR used in our clean room facilities for PMG fabrication, some rapid studies were made to access PR resolutions. Utilizing both positive and negative PRs, the analysis started by 10 μm linewidth dimensions (sub-10 μm lines are imperceptible to the human eye [6]), down to the highest resolution the DLW equipment is able to achieve, *i.e.*, 600 nm. Below in **Table 1**, we can observe that the smaller the pattern, the smaller the resolution. The larger structures were easily reproduced and appear to be quite consistent. However, 600 nm patterns look more undefined, namely in the junctions, which is very evident in the negative PR. The intermediate linewidth, 1 µm, appears to be appropriate considering the high resolutions we aim to achieve. Additionally, still in 1 µm features, it is possible to observe that in the negative PR image, there is a periodical deviation in the vertical lines of the PMG. This is due to artifacts of the DLW equipment, and not due to the PR nor to the mask design, and it occurs occasionally.

Table 1 – Positive and negative photoresist patterns with different dimensions analyzed with SEM.

Linewidth	**Positive photoresist**		**Negative photoresist**	
10 µm	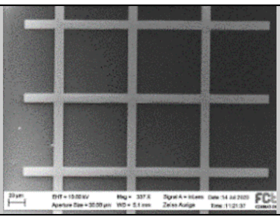	Linewidth = NA Spacing = NA	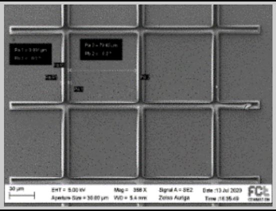	Linewidth = 9.9 µm Spacing = 79.6 µm
1 µm	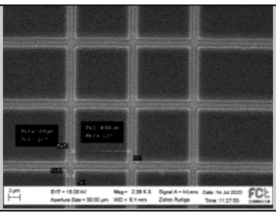	Linewidth = 1.1 µm Spacing = 9.9 µm	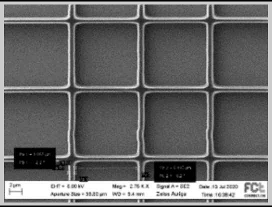	Linewidth = 1.1 µm Spacing = 9.9 µm
600 nm	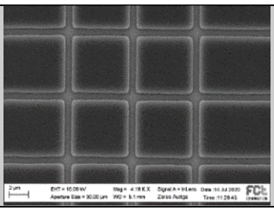	Linewidth = NA Spacing = NA	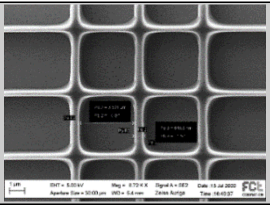	Linewidth = 648 nm Spacing = 3.5 µm

3.3 Patterning Gold PMGs

This section comprehends the patterning processes studied, namely gold wet etching and acetone lift-off.

3.3.1 Control Mask Layout

Initially, a control mask was designed in KLayout (**Figure 3.2**), and used to pattern and study the structures we want to fabricate. It considers the PMG previously produced in another study with a linewidth of 10 µm and a spacing of 80 µm [37], followed by smaller PMGs whose dimensions and density we aim to achieve, and some simple lines to test the capacity of the patterning process as well as the resolution capacity of the DLW equipment. DLW has a maximum resolution of 600 nm, and the smaller PMGs have a linewidth with the same dimension, but with different spacings and, consequently, different line densities.

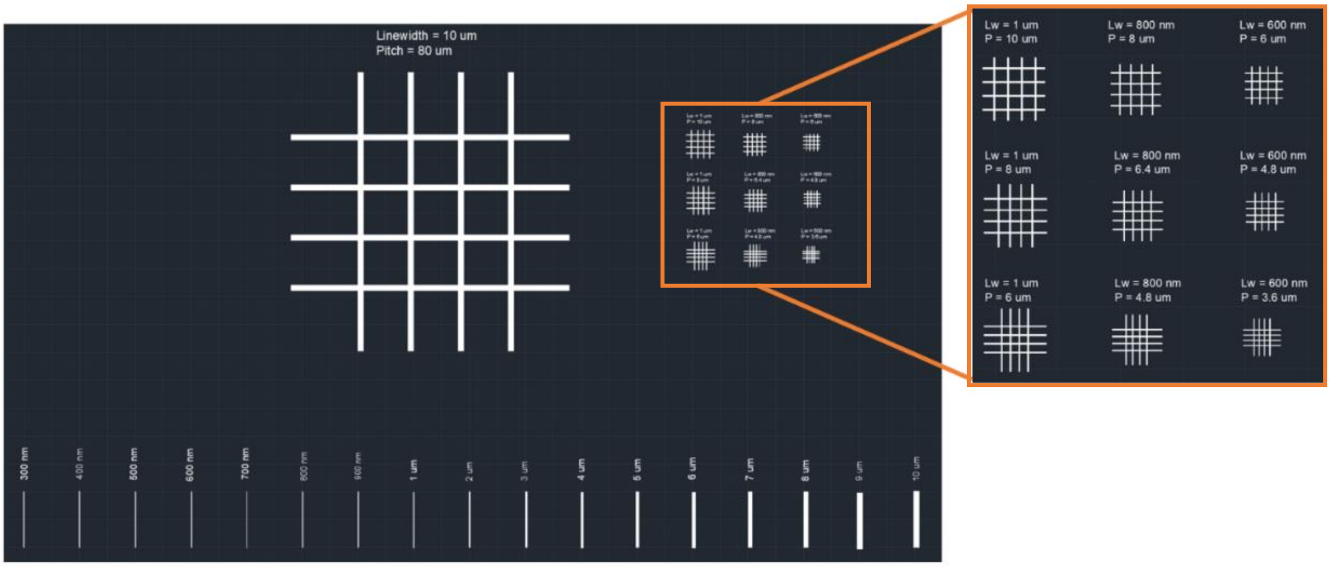

Figure 3.2 – Control mask layout with different PMG dimensions and a gradient of linewidths.

3.3.2 Wet Etching

As a first approach, gold wet etching tests were performed. The followed protocol can be found in **Appendix D**. Depicted in **Table 2**, it is possible to observe that gold is etched after 4 minutes, remaining only a titanium thin film, which functioned as the adhesion layer to the substrate. When the sample was observed under the optical microscope, several particles of gold (maybe nucleation sites from the E-Beam gold deposition [63]) persisted on the sample, even when longer times of wet etching were applied, as shown in **Figure 3.3**.

Table 2 – Wet etching effect on a sample over 4 minutes.

0 min	1 min	2 min	3 min	4 min
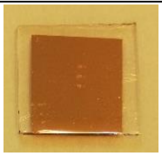	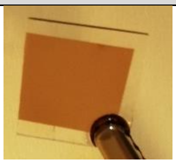	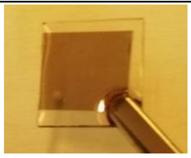	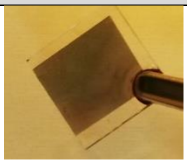	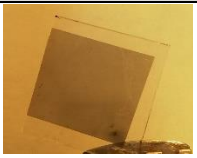

After a few trials, it was clear that the PMGs and lines normally disappeared from the sample in the first two to three minutes, which indicates they do not withstand the wet etching process. This may be due to thickness variability of the gold deposition in the E-Beam system and a constant erosion rate at 40 nm/min (see **Appendix E**, where the gold thickness was measured), which makes any etching process that considers these lateral resolutions unfeasible. Despite of the majority of the structures vanish in the first minutes of wet etching, some structures in some of the samples lingered on the substrate and often resembled as in **Figure 3.3**, where the remaining gold particles are prevalent. Nevertheless, wet etching was an extremely variable process throughout testing, and we decided to evaluate lift-off.

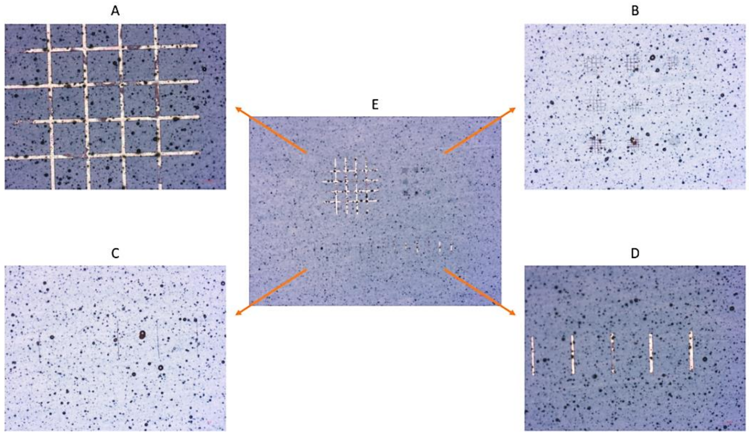

Figure 3.3 – Structures after wet etching 4-minute process observed under the optical microscope. A) PMG with larger feature sizes; B) PMGs whose sizes we want to achieve; C) Smaller lines, being the smaller one 600 µm wide; D); Larger lines (6 µm to 10 µm of linewidth); E) Mentioned structures altogether.

3.3.3 Lift-off

By observing **Figure 3.4**, the lift-off result looks almost identical to the control mask layout. Even though this process is longer than wet etching (it can take a few hours) and showed a low yield, *i.e.*, the quantity of resulting samples was very low, it removed the titanium and gold layers from the unwanted places much more easily and efficiently than wet etching. Also, the resulting samples are much cleaner, and the process does not require special chemicals, such as gold etchant, it only requires acetone to dissipate the positive photoresist below the metal. Additionally, the gold in the structures does not look uniform due to graphite impurities in the gold crucible during metal deposition on the E-Beam system. The larger structures, such as the large PMG and the wider lines, were very easy to manufacture due to their dimensions. However, when downsizing the structures and increasing line density, the process reproducibility and yield decreased a lot. Particularly, the denser structures, as the smaller PMGs, are rather difficult to obtain since they require more soft brushing in order to remove the remaining material between the lines. Nevertheless, this method was the selected one to proceed with PMG fabrication due to the advantages it offers when compared to gold wet etching.

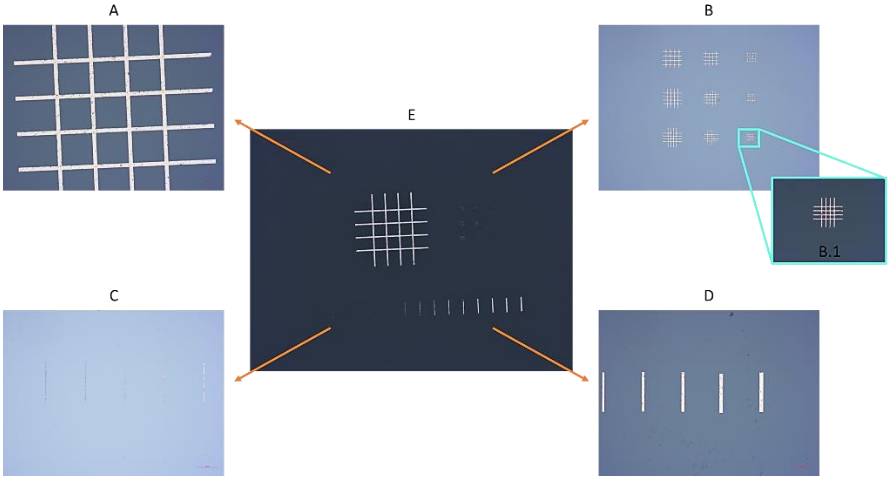

Figure 3.4 – Structures after lift-off method under the optical microscope. A) Structure with larger feature sizes; B) PMGs whose sizes we want to achieve; C) Smaller lines, being the smaller one 600 µm wide; D); Larger lines, having the wider one 10 µm of linewidth; E) Mentioned structures altogether.

3.4 PMG Linewidth

3.4.1 Optical Proximity Effect

In order to assess the influence of line density within a PMG and how accurately PMG features were reproduced during the photolithographic processes, we studied the proximity effect [64]. Considering the 10 µm PMG, since the spacing is very small and the lines are very close to each other, it is expected that the proximity effect is slightly more accentuated. On the other hand, in the PMG with 22 µm of spacing, the features are distant from each other, therefore a minor proximity effect is foreseen. For this study, linewidth measurements were made using optical microscopy and SEM images. The results are shown in **Table 3**.

Table 3 – Proximity effect analysis in positive photoresist patterned grid and gold PMG (20 measurements per image) for 1 µm of linewidth.

Spacing	Image acquisition equipment	PR PMG		Gold PMG	
		Image	Linewidth	Image	Linewidth
10 µm	Optical Microscope	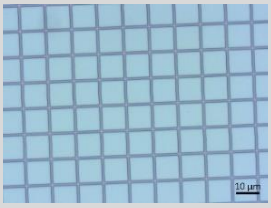	0.9 ± 0.5		1.2 ± 0.1
	SEM	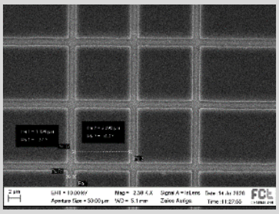	1.07 ± 0.06	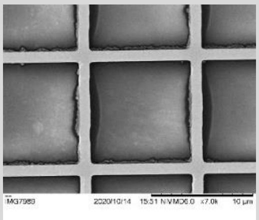	1.02 ± 0.03
22 µm	Optical Microscope	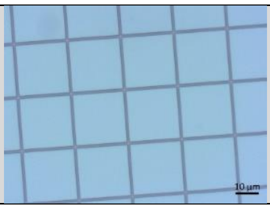	0.96 ± 0.05	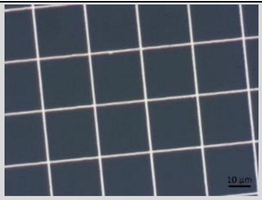	1.11 ± 0.06

Regarding the results in **Table 3**, the values were taken from ImageJ software. The values acquired from the SEM micrograph are more precise than those from the optical microscope, given the resolution of the equipment, thus the SEM results are closer to the established linewidth value of 1 µm. Nevertheless, comparing both PMG results, we can assume that proximity effect is negligible. Therefore, there is almost no interaction of the laser photons with the photoresist and substrate (through back-scattering) and, consequently, no need to adjust the laser dose. Maybe if the spacing between lines was smaller (larger density), we would observe such effect.

3.4.2 Linewidth Study

As for the linewidth resolution, the considered linewidth for PMG fabrication and analysis was 1 µm and this dimension was the wider one we wanted to consider. Afterwards, some trials on decreasing the linewidth were made, namely with 800 nm of linewidth. However, these lines did not withstand the process, as we can see in **Figure 3.5 A)**, where PMG lines are not as robust as in **Figure 3.5 B)**. Thus, we continued to conduct our studies using 1 µm of linewidth.

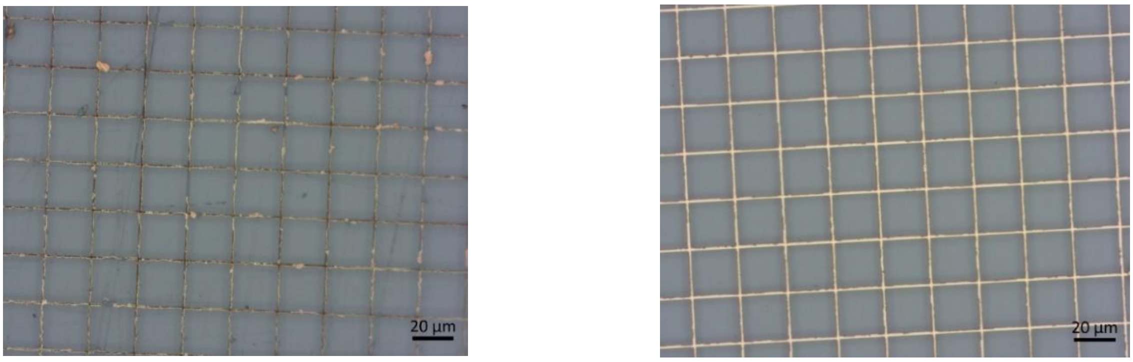

A **B**

Figure 3.5 – Comparison between linewidths. A) Gold PMG with 800 nm of linewidth; B) Gold PMG with 1 µm of linewidth.

It was possible to extract some results of the gold PMGs above. Both PMGs have a spacing of 10 µm, only varying the linewidth. The sheet resistance slightly increases when diminishing linewidth, due to the less metal there is in the 800 nm PMG. Transmittance increases approximately 5%.

Table 4 – Optical and electrical PMGs characterization, considering a decrease in linewidth, with a constant spacing of 10 µm.

Linewidth	Sheet Resistance (Ω/sq)	Transmittance (%)
1 µm	3.40	68.48
800 nm	3.91	73.44

3.5 PMG Characterization

3.5.1 PMG Simulation

In order to assess the dimensions that would offer an optimal trade-off between sheet-resistance and transmittance, we started by simulating PMG properties in COMSOL Multiphysics (sheet resistance) and in Ansys Lumerical – FDTD Solver (transmittance).

In **Figure 3.6**, taken from COMSOL software, we can see the current flow through the PMG. While horizontal lines are in bright orange, representing very high current density, vertical lines are dark blue, illustrating a low current flow. This is due to the fact that, in the simulation, the voltage was applied on the first vertical line of the PMG on the left, as shown in **Figure 3.6**, but in reality each PMG electrode is in conformal contact with the brain surface, therefore current flow will be more homogeneous.

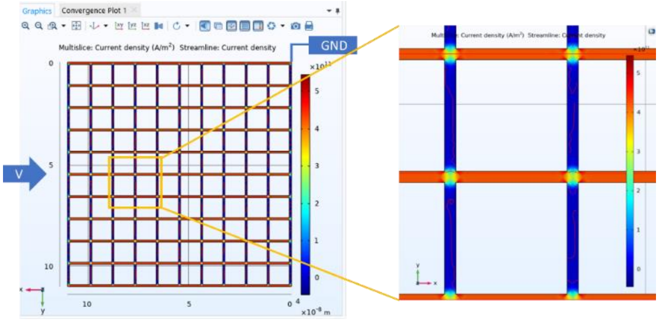

Figure 3.6 – Current density represented in false colors through COMSOL Multiphysics.

Regarding how FDTD simulations were made, since we have applied a periodic condition due to the periodic nature of the PMG, considering the period as one square, the FDTD region will only assume the area of that square, resulting in shorter simulation times. Moreover, the assumed small thickness of the glass substrate (600 nm) is here very well represented when compared to the 80 nm thickness of the gold PMG.

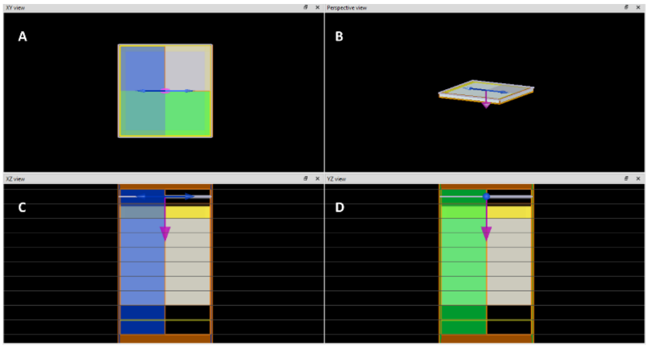

Figure 3.7 – Schematic of the PMG simulation structure on Ansys Lumerical - FDTD Solver, with the goal of obtaining simulational results for PMG transmittance. A) XY view; B) Perspective view; C) XZ view; D) YZ view.

3.5.2 Comparison of Simulation with Experimentation

Attending to the simulation values, they do not differ very much from the results obtained in the laboratory (see **Table 5**). Regarding the sheet resistance values, both simulation and experimental results are very similar. However, transmittance values obtained in simulations somewhat diverge from experimental results. This can be due to the thickness of the glass considered in the simulation, since in reality the glass thickness is around 1 mm and in simulation is 600 nm. Additionally, in the software, glass is assumed as an inert material, having a zero-absorption value, while in reality glass actually has a small parasitic absorption. This small thickness was used to reduce processing time. For instance, if we tried to simulate PMGs with the real glass substrate thickness, the simulation could take days or even result in error after long hours of computation.

In the first columns of **Table 5**, the density of the fabricated PMGs diminishes as the spacing between the lines increases, thus resulting in a rise in transmittance values. However, lesser the lines, lesser the material for conduction electrons to flow, which results in an increase of the sheet resistance. The best value we found regarding this interplay was a spacing of 22 µm between lines.

Moreover, the further we go in increasing the spacing, the higher the values in sheet resistance as well as in transmittance, but there is also one parameter to consider: the number of lines inside the electrodes, which in this work will have 500 µm of diameter. If there is not a sufficient amount of lines in the electrode to capture neural signals, then the electrode impedance will be too high. Therefore, 22 µm of spacing was the optimal threshold found between these three criteria (good sheet resistance, transmittance, and sufficient number of lines within the electrode).

Table 5 – Optical and electrical PMGs characterization obtained through experimentation and through simulation, considering an increase in spacing (from 6 µm to 22 µm, with a constant linewidth of 1 µm).

Spacing (µm)	**Gold PMG**	**R_S (Ω/sq)**		**T(%)**	
		Lab	**Sim**	**Lab**	**Sim**
6		1.99	1.70	60.40	70.56
8	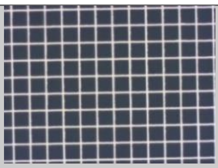	2.19	2.21	64.44	76.11
10	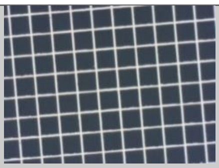	3.40	2.71	68.48	79.78
12	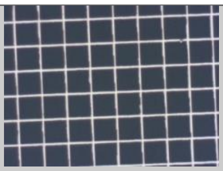	4.18	3.22	72.14	82.35
14	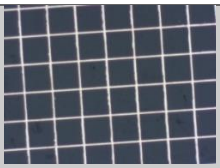	4.39	3.72	74.50	84.25

20	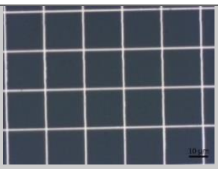	6.27	5.24	80.4	87.81
22	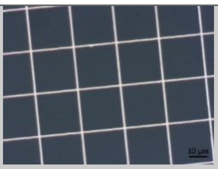	**6.65**	**5.74**	**81.01**	**88.61**

In **Figure 3.8 A)**, it is possible to compare simulational and experimental spectra in the range of visible light (400 nm to 700 nm) of the selected PMG with 22 µm of spacing. Both exhibit approximately the same behavior, being the experimental spectrum a bit more rough. The same happens when comparing transmittance and sheet resistance results in **Figure 3.8 B)**, the simulation curve is more smooth whereas the experimental one is more irregular. This is due to the fact that experimental conditions are never ideal resulting in uneven outcomes.

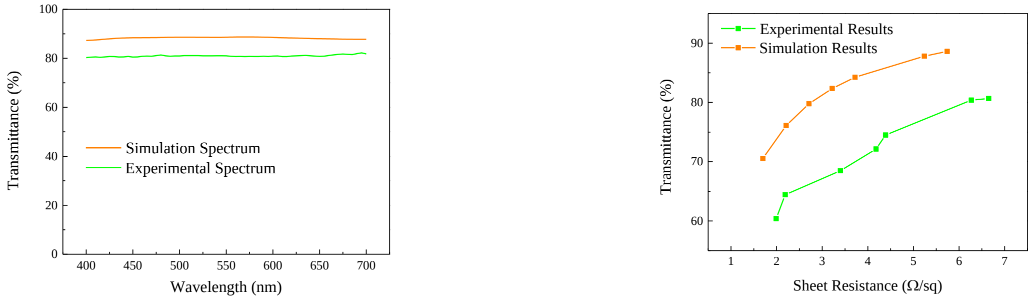

A

B

Figure 3.8 – Simulational and experimental results comparison. A) Transmittance spectra comparison; B) Transmittance and sheet resistance results comparison.

3.5.3 Comparing PMGs with TCOs

Comparing these values to ITO, for the same thickness of 80 nm as in our PMGs, its sheet resistance is around 70 Ω/sq [65], which contrasts with the obtained sheet resistance of the selected PMG of 6 Ω/sq (1 µm of linewidth and 22 µm of spacing), and its transmittance is 82%, close to the chosen PMG transmittance of 81%, for a 550 nm wavelength. As for IZO, another well-known TCO, we studied its transmittance spectrum for a 200 nm thickness, and compared to our PMG (**Figure 3.9**). The values of transmittance at 550 nm are 81% for the gold PMG, as mentioned before, and 77% for this sample of IZO. Additionally, the value of sheet resistance for our PMG is approximately 6 Ω/sq, and for the considered IZO sample is 25 Ω/sq. By comparing the spectra, we can infer that in a wide range of the light spectrum, the PMG has a much more steady behavior than IZO, which has a very irregular one (interference fringes), namely in the visible range. This means that in this range the PMG will maintain its transparency constant. Being transparent for optical imaging is important because it means that a large percentage of light is transmitted through the film in both directions, enabling excitation and light emission in return.

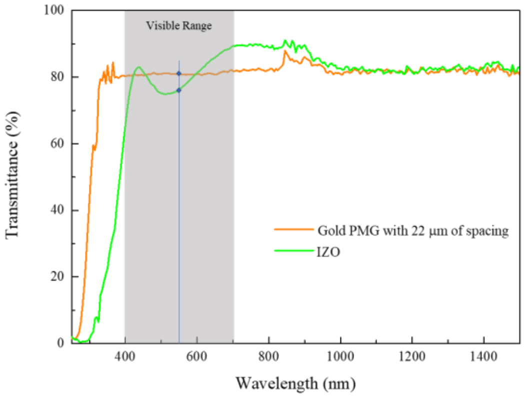

Figure 3.9 – Transmittance spectra of an IZO sample (200 nm thick) and of the selected gold PMG, with the visible range denoted.

3.5.4 Gold Structural Characterization

Attending now to gold itself, this metal in bulk form is typically polycrystalline. When evaporated via electron-beam and deposited onto the sample surface, individual islands of gold (as seen in **Figure 3.3** during wet etching tests) will grow in size, coalesce and the thin film becomes structurally continuous [66]. According to the diffractogram below, obtained by X-Ray Diffraction (XRD), Miller indices (hkl) indicate that the prevalent crystalline plane is at (111), with large gold crystallites, suggested by the peak height, and smaller peaks at 77 and 82 show the presence of planes at (311) and (222), respectively, indicating smaller gold crystallites with these crystallographic directions. **Figure 3.10 B)** shows the gold irregular surface morphology, and also some debris from the lift-off process in the side walls of the PMG.

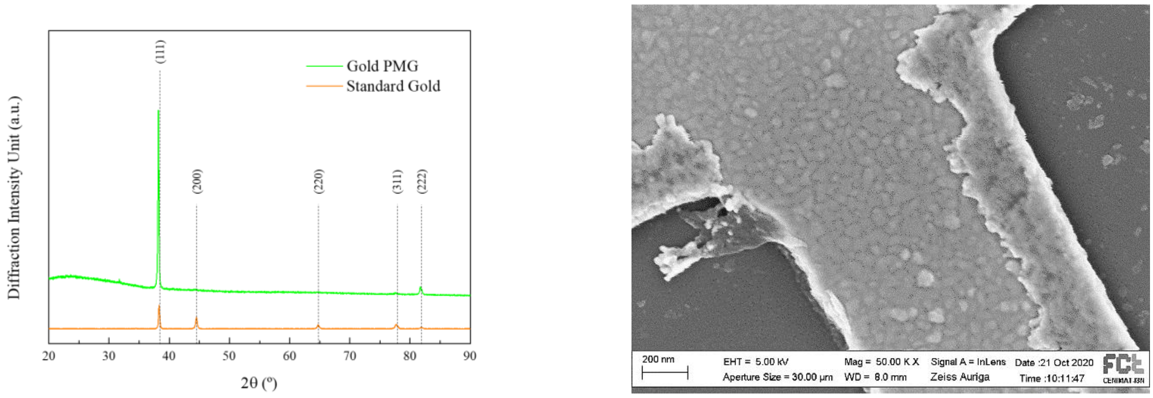

A **B**

Figure 3.10 – Structural analysis of the gold used in PMG fabrication. A) X-Ray diffractogram, plotting the diffraction intensity as a function of the angle (measured in 2Θ) collected from a gold PMG and compared to a standard gold diffractogram [67] (a.u. – arbitrary units); B) SEM image of a PMG partial line, where surface morphology is evident.

3.6 PMG Production on Parylene-C

This section comprehends PMG fabrication on a flexible Parylene-C substrate, including the exploration of an additional step of oxygen plasma, and flexible PMG characterization.

3.6.1 Oxygen Dry Etching as a Pre-treatment

Until this moment, all of the aforementioned PMGs were fabricated on a glass substrate. However, since this specific application lies within the scope of flexible electronics, we started producing the PMGs on Parylene-C. The yield of PMG fabrication on a glass substrate was very low, but the yield on a Parylene-C substrate was even lower. Therefore, we found a way to overcome this problem which was to apply oxygen dry etching to the sample before the gold deposition. In this manner, the oxygen plasma would remove the residues of PR still present on the sample that the developer could not, and, depending on the time of this step, oxygen can also start to etch Parylene-C, creating surface roughness and, therefore, increasing polymer-metal adhesion [68], [69]. Surface roughness in this specific application is welcomed since it increases electrode contact with the living tissue from the brain surface, improving signal quality.

After the gold deposition, we observed that the gold had a brownish color (as depicted in **Appendix G**), but was still conductive. Our approach was to analyze its surface roughness in AFM (Atomic Force Microscopy). We submitted six Parylene-C samples (on a glass substrate) to different oxygen dry etching times, and lastly deposited gold. The results are on **Table 6**, and it is evident an increase of the surface roughness over time. Very dark and very bright spots are shown in the last picture which, according to the scale bar on the right, indicate the RMS roughness (Root Mean Square), *i.e.*, the surface height. Recalling the thickness of the Parylene-C substrate (5 µm), and considering this amount of surface roughness (71.7 nm), the 6 nm of titanium and the 80 nm of gold must have been deposited in a conformable manner to Parylene-C rough surface. Therefore, gold instead of being yellow and shiny, which is caused due to a large amount of light being reflected in a specular direction, presented a brown and dim color since there is no specular light being reflected, only diffuse light, which is reflected in every other direction. Hence, gold color changing is most likely just an optical effect.

Table 6 – Atomic force microscope scans showing oxygen plasma pre-treatment effects on Parylene-C and gold surface roughness.

O_2 Plasma Treatment Time	**0 min**	**1 min**	**2 min**	**3 min**	**4 min**	**5 min**
Gold in Parylene-C	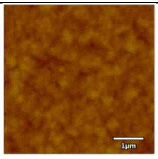	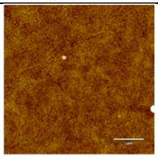	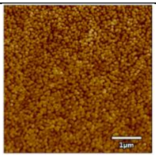	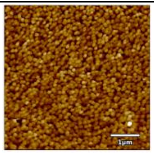	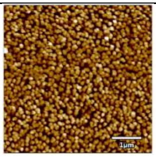	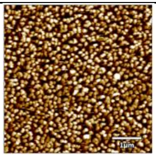
RMS (nm)	8.4	15.1	25.9	33.4	53.8	71.7

Subsequently, we wanted to know how this process influenced the sheet resistance of a gold thin film. In **Figure 3.11**, a small increase in this parameter is observed. When the sample is submitted to oxygen plasma, the plasma will create surface roughness on the Parylene-C that is not covered by the PR structures, as mentioned before. Afterwards, gold will be deposited on Parylene-C with a rough surface, thus also assuming high surface roughness as observed in **Table 6**. Materials with nanometric dimensions intrinsically exhibit higher electrical resistivity due to additional scattering centers for the conduction electrons, mainly from surfaces and grain boundaries [63]. Therefore, if the surface roughness is increased, there will be more scattering centers for electrons to collide, and the sheet resistance, dependent on the material resistivity, will rise (see **Equation 1**). Moreover, we can see that this increase seems to stabilize after 2 minutes of oxygen plasma dry etching. This is due to the fact that roughness-induced resistivity only increases considerably when the roughness is larger than the *de Broglie* wavelength of electrons, which we can confirm by looking at **Table 6** and observing that roughness only becomes substantial after 2 minutes [70].

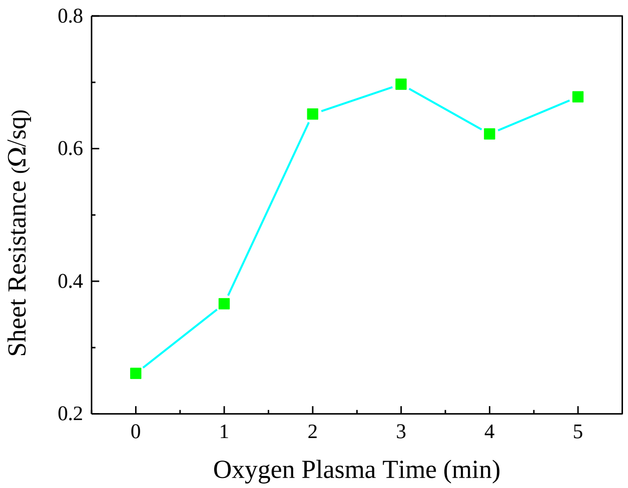

Figure 3.11 – Different times of oxygen dry etching pre-treatment and its effect on the sheet resistance of an 80 nm thin film of gold.

In **Table 7**, sheet resistance values of the gold thin film on different conditions can be seen. The theoretical value for sheet resistance was obtained through **Equation 1**, where ρ is the material resistivity, L is the length, W is the width, and t is the sheet thickness. The experimental and simulation values are identical to the theoretical value. With 5 minutes of oxygen dry etching pre-treatment, the sheet-resistance increases approximately by 140%.

Nevertheless, this change in sheet resistance is not significant when comparing to the advantage that O_2 plasma treatment brought to the process: significantly increasing the yield, obtaining around 90% of adequate samples. The underlying reason for this considerable increase in yield is that, since metal-polymer adhesion is improved, we can perform the lift-off process in ultrasonic bath of acetone, easily removing the unexposed PR and the metal on top. Hence, the lift-off process time decreases from long hours to a few minutes.

Table 7 – Gold thin film sheet resistance values on different conditions. The gold thin film is 80 nm thick.

	Theoretical Value	**Simulation Value**	**Experimental Value**	**With 5 min of O_2 plasma**
R_S (Ω/sq)	0.28	0.28	0.28	0.68

$$R_S = \rho \frac{L}{Wt} \qquad \textbf{Equation 1}$$

When the sample is submitted to oxygen dry etching, oxygen plasma not only removes PR residues from the development step, but it will also remove some PR from the side walls of the patterned structures, as well as create surface roughness in the Parylene-C that is unprotected by the structures, *i. e.*, inside the lines. In such manner, linewidth can slightly increase due to this intermediate step. Depicted in **Figure 3.12**, a sample with PR structures was half exposed to oxygen plasma, and the other half was covered. The region without this treatment showed a linewidth of 1.044 µm, later confirmed in ImageJ software (1.1 ± 0.1 µm), whereas a value of 1.441 µm (1.4 ± 0.1 µm in ImageJ) for the area that suffered this treatment was attained. Therefore, we can conclude that this step increases linewidth approximately by 27%.

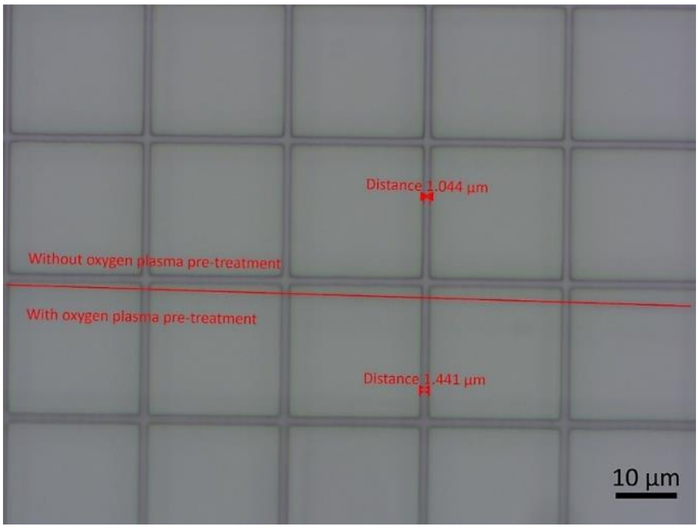

Figure 3.12 – Effect of oxygen dry etching in the linewidth (1 µm) of PR patterned structures. The top half did not suffer any treatment. The bottom half was submitted to 5 minutes of oxygen plasma.

After the gold deposition and ultrasonic lift-off process, the linewidth of the gold PMG was measured, showing a value of 1.4 ± 0.1 µm. Below, it is possible to observe that the sample region that was not exposed to oxygen plasma is completely absent, while the region submitted to this treatment is very uniform. Therefore, we can conclude that this step was crucial during PMG electrode manufacturing process.

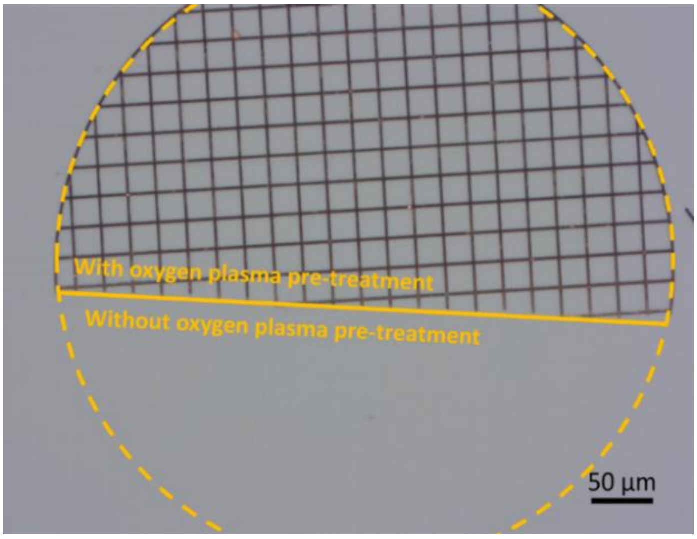

Figure 3.13 – Effect of oxygen dry etching pre-treatment on PMG on Parylene-C. It is possible to see that without this step the gold PMG does not adhere to the substrate.

3.6.2 Bending Tests

In order to determine the liability of the flexible PMG, bending tests with ~ 5 mm of diameter were performed. The ratio of the change in PMG sheet resistance recorded as a function of the bending cycle is demonstrated in **Figure 3.14**. Here, it is shown that the sheet resistance of the PMG with 22 µm of spacing almost does not change with the consecutive bending cycles. This is due to the ductility of gold and the mechanical robustness of the Parylene-C substrate. Therefore, the sample exhibits a stable electrical performance, even after more than 1000 bending tests. Nevertheless, this bending test represents an extreme situation, since during neural recordings from the cerebellum, the curvature is smaller (larger bending diameter) and the electrodes are implanted in a fixed position [1].

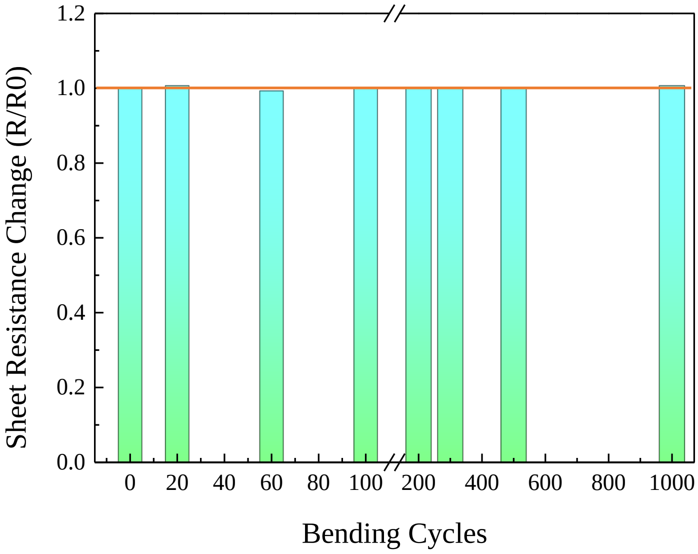

Figure 3.14 – Testing sheet resistance variation of gold PMG during bending cycles. Histogram bars that surpass the orange line represent a sheet resistance change (R/R0) superior to one.

3.7 ECoG MEA Production

After PMG study and selection, fabrication and characterization of the PMG in Parylene-C flexible substrate, we finally proceed to prototype production. The electrodes were fabricated considering the gold PMG with 22 µm of spacing and 1 µm of linewidth. Each electrode has a diameter of 500 µm, and the MEA have 16 electrodes distributed over 3 mm. This ECoG has a round shape with 3 mm of diameter because we are limited by the cranial window size, which is equally 3 mm wide, thus taking advantage of the available area.

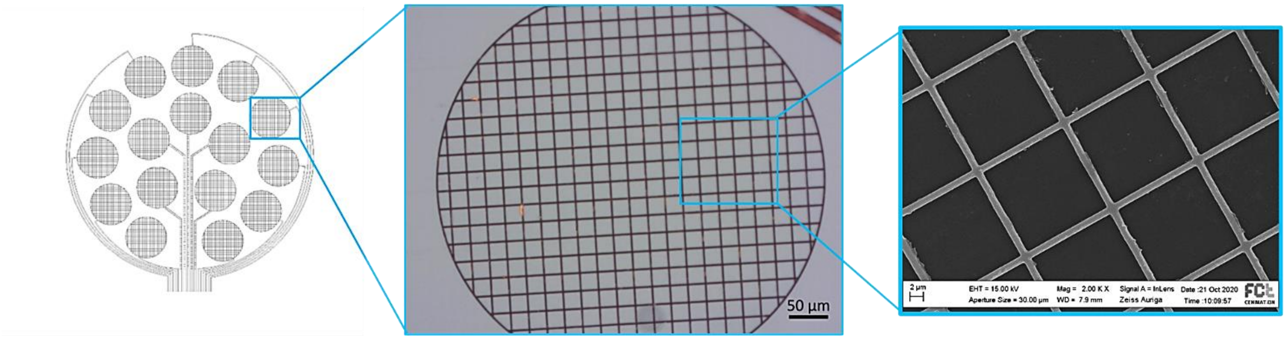

Figure 3.15 – Prototype with 16 gold PMG electrodes. In the first image we can see the head of the device, showing its 16-electrode configuration as well as the metallic vias, followed by an image of one PMG electrode. Lastly, a SEM micrograph of the gold PMG is demonstrated.

The entire prototype has around 3 cm of length and consists of three main components: the head of the device with 16 electrodes, the metallic vias, and the connection pads to connect to the ZIF adapter. The Parylene-C substrate is 5 µm thick, and Parylene-C for encapsulation is 1.5 µm thick. In **Figure 3.16**, we can see a picture of the device (**Figure 3.16 A**), next to a microscope image of the center of the head showing the transparent electrodes (**Figure 3.16 B**). It is noteworthy that crosstalk between metallic vias was not observed.

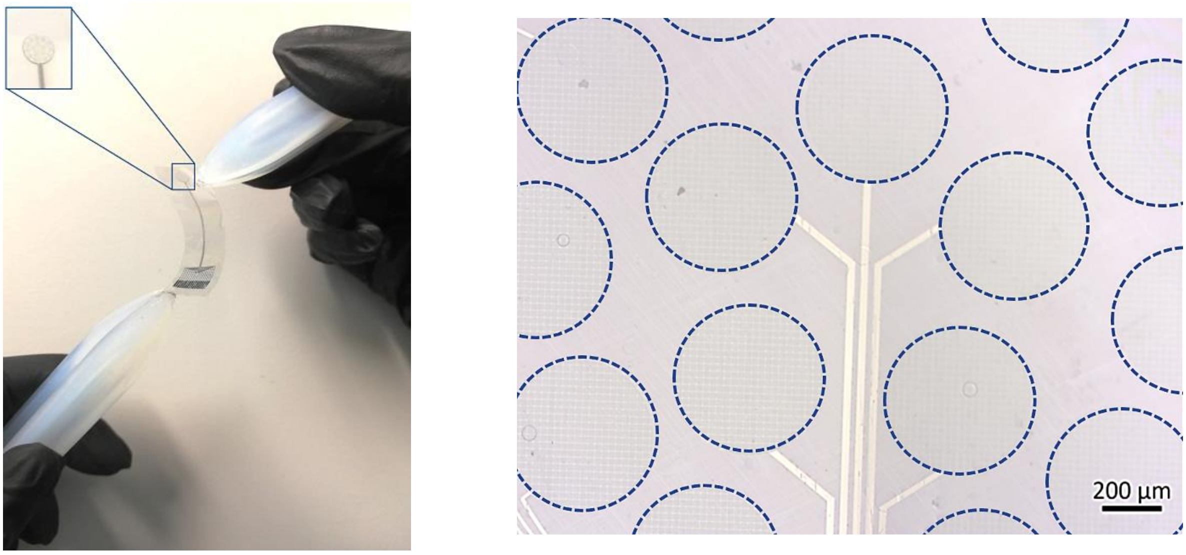

A **B**

Figure 3.16 – Transparent and flexible ECoG MEA prototype. A) Picture of the flexible ECoG prototype; B) Transparent gold PMG electrodes denoted with blue dashed lines.

3.8 ECoG MEA Characterization

The final step of this work was to test the ECoG MEAs *in vitro* through Electrochemical Impedance Spectroscopy (EIS), and *in vivo* on mouse cerebellum.

3.8.1 *In Vitro* Characterization

Impedance analysis at 1 kHz is a common metric to determine how a specific ECoG device will perform *in vivo*. A few measurements were made, and the final values were calculated by averaging the data of the channels correspondent to the electrodes. The standard deviation was also determined at this time. The obtained results from the final prototype and from the control prototype (whose electrodes consist of a plain thin film of gold with 80 nm of thickness, instead of a gold PMG, as illustrated in **Appendix H**) are shown in **Table 8**, where we can see that low-impedance devices were attained.

Table 8 – Impedance results for the final prototype and for the control prototype, with 500 µm of diameter electrodes.

Control Prototype Impedance	2.08 ± 0.02 kΩ
Final Prototype Impedance	13.10 ± 0.07 kΩ

In **Figure 3.17**, it is possible to observe impedance magnitude measured at 1 kHz in saline as a function of different electrodes and prototypes. The points denote impedance magnitude measured at 1 kHz in saline solution for individual electrodes, and the boxplots show the distribution of these values.

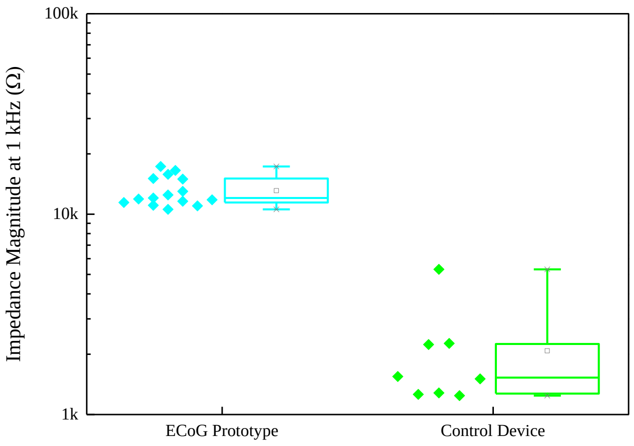

Figure 3.17 – Impedance magnitude measured at 1 kHz in saline solution.

In **Table 9**, we summarized the transmittance, sheet resistance, impedance values, electrode materials and its dimensions to illustrate the trade-off between those parameters. We also benchmarked the performance of the fabricated electrodes against previous transparent electrodes. The key parameters that govern the utility of ECoG transparent electrodes are the transmittance and sheet resistance, as well as the impedance at 1 kHz. By observing these values below, we can infer that the impedance we achieved is one of the lowest, and the trade-off between sheet resistance and light transmission was also well attained. When compared to graphene for instance, transmittance is normally very high, but it comes with the cost of increasing impedance. The same happens with ITO, so research groups are betting on hybrid structures in order to find an interplay between the advantages and drawbacks that each material offers. Nevertheless, the obtained results from our electrodes put us in a prominent position in the current state-of-the-art.

Table 9 – Current transparent electrodes and their dimensions, impedance magnitude at 1 kHz in saline solution, sheet resistance and transmittance value at 550 nm. (NA: Not Available; ⦸: Diameter)

Reference	Electrode Material	Electrode Dimension	|Z| @ 1 kHz	Sheet Resistance (Ω/sq)	Transmittance @550 nm
[4]	Doped Graphene	50 x 50 µm	~ 500 kΩ	NA	90 %
[71]	Graphene	100 x 100 µm	15 kΩ	NA	50 %
[41]	Graphene	200 µm ⦸	243 kΩ	76	90 %
[5]	Graphene	100 x 100 µm	> 963 kΩ	NA	90 %
[72]	CNT	NA	0.2 MΩ	150 – 500	70 – 90 %
[44]	PEDOT:PSS	30 µm	46.5 kΩ	NA	93 %
[38]	TiN	30 µm ⦸	510 – 590 kΩ	41 – 199	18 – 45 %
[3]	ITO	250 µm ⦸	10 – 50 kΩ	200	62 %
[73]	ITO	80 µm ⦸	250 kΩ	NA	80 %
[40]	ITO	500 µm ⦸	300 kΩ	43.7	90 %
[39]	IZO 200 nm	500 µm ⦸	40.7 kΩ	25	76 %
	AgNWs + IZO	500 µm ⦸	23 kΩ	23	74 %
[58]	Au Grid + PEDOT	80 x 80 µm	11 kΩ	NA	70 %
[36]	Au Grid	80 x 80 µm	127 kΩ	18	70 %
[74]	AuNW	200 µm ⦸	33.9 kΩ	3 - 20	81 %
[37]	ITO + Au PMG	NA	5.4 – 18.4 kΩ	5.6 – 14.1	59 – 81 %
Our work	**Au PMG**	**500 µm ⦸**	**13 kΩ**	**6**	**81 %**

3.8.2 *In Vivo* Characterization

Neural data was acquired from a mouse cerebellum surface using these transparent ECoG MEAs. These tests were conducted on anesthetized mice. **Figure 3.18 A)** shows the setup to fix the mouse's head in order to implant the device. **Figure 3.18 B)** demonstrates the transparency of the electrodes and the ability to visualize the underlying cerebellum and vasculature through the prototype. **Figure 3.18 C)** shows the control device. The difference between the last two images is clear due to the transparency of the electrodes. The prototype showed a perfect adjustment to brain surface and the process of placing and fixing the prototype is feasible and compatible with the cranial window needed for imaging, demonstrating its compatibility with the imaging protocol.

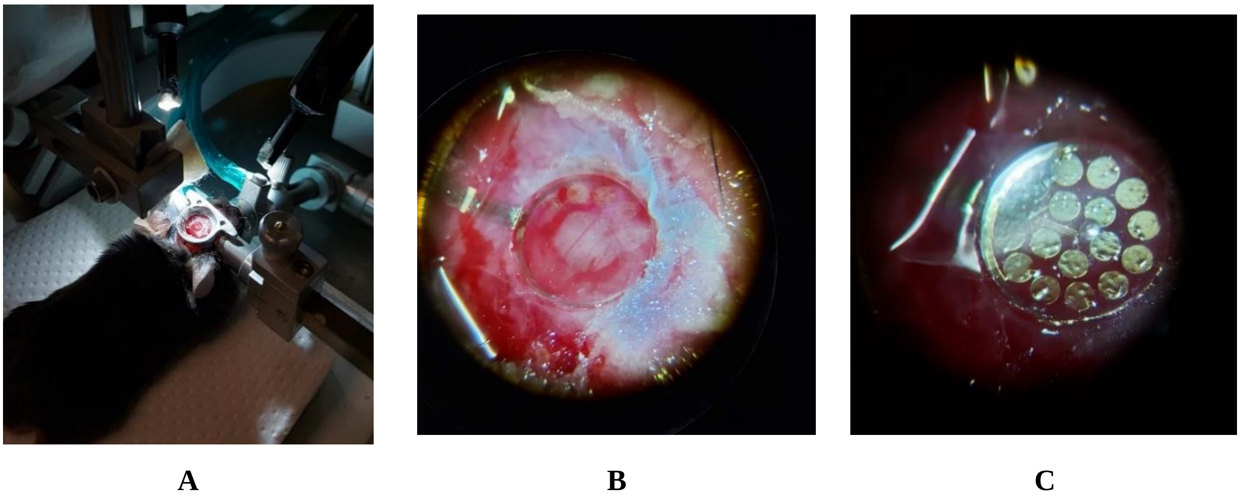

Figure 3.18 – Pictures from implantation surgery. A) Head-fixed setup for device implantation; B) Transparent and flexible ECoG MEA; C) Control prototype whose electrodes are made of a simple gold thin film.

After implanting the ECoG MEA, the mouse was positioned in the behavior and imaging setup where the animal is walking on a round treadmill, as shown in the scheme of **Figure 1.2**, and as depicted in **Figure 3.19**.

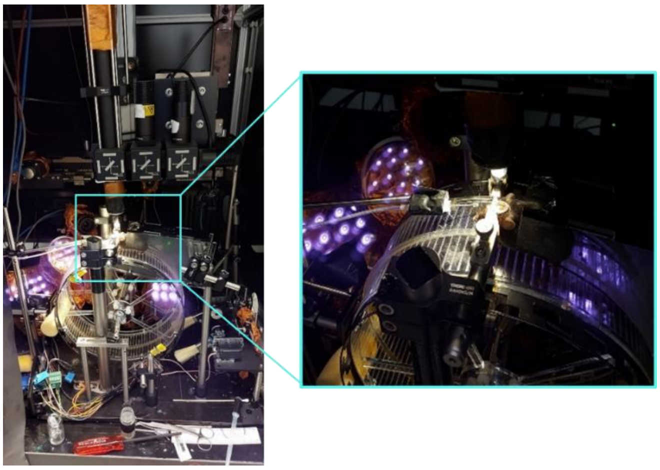

Figure 3.19 – Mouse positioned on the behaviour and imaging setup with the device implanted in its cerebellum.

3.8.3 Neural Data Analysis

Figure 3.20 shows the neural data acquired during mouse walking on the treadmill at the time of movement trigger. It is possible to observe four electrodes with high amplitudes and high signal to noise ratio (SNR). Simple spikes in Purkinje cells, which are located in the cerebellar surface and are involved in mouse movement, are modeled by the movement of the paws, therefore, these signals may be signs of locomotion. However, such has to be confirmed in the future with behavior analysis.

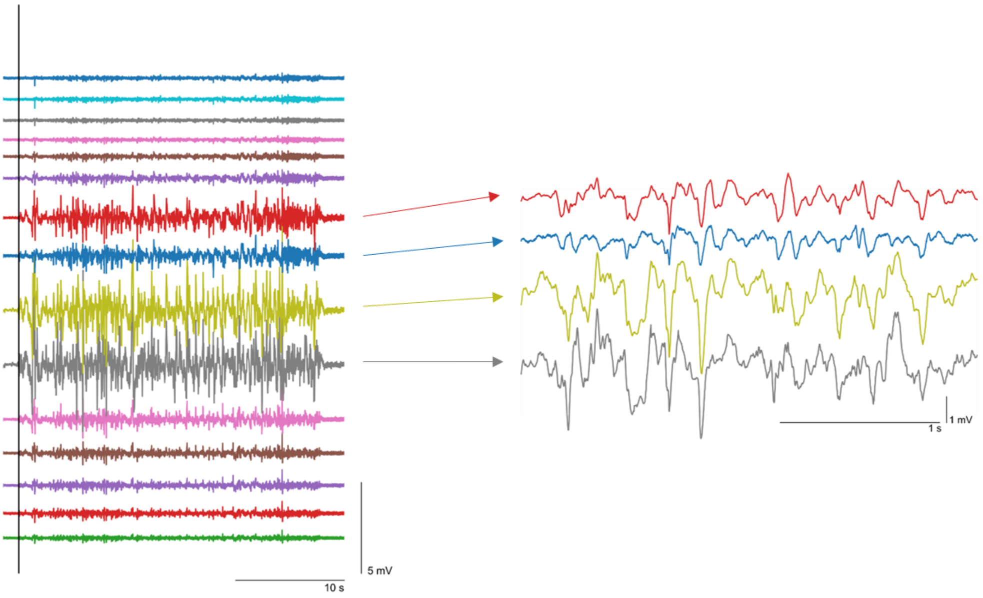

Figure 3.20 – Neural data acquired during mouse walking on treadmill at the time of movement trigger.

Through these preliminary tests, it was possible to measure signals from putative Purkinje cells. In this manner, we validate ECoG MEAs for electrical signal acquisition.

4. Conclusions and Future Perspectives

The field of neuroengineering has been evolving due to the advantages it offers, both for neuroscience research and for clinical applications. The more researchers are able to get data from the brain, the more we will understand this organ as well as the diseases affecting its normal functioning. A way to obtain neural information is by using conductive electrodes to measure neurons' electrical activity. However, we have to consider that the quality of the signal is dependent on how close our electrodes are to the object under study (**Figure 1.1**). Therefore, ECoG recordings are a promising way to obtain neural information and, by using functional calcium imaging as an auxiliary tool, data with high temporal and spatial resolution will be attained (**Figure 1.2**).

In this project, we developed a flexible ECoG prototype with transparent electrodes, in which the gold PMG, the key element of these electrodes, was exhaustively analyzed, since PMGs are a promising candidate for TCEs nowadays (**Figure 1.4**).

We started by analyzing the linewidth of the PMG. DLW equipment has a maximum resolution of 600 nm. However, the minimum feature size that showed to be reliable and to withstand the process, especially the lift-off steps, was 1 µm of linewidth (**Figure 3.5**). Thus, we conducted our studies with this dimension. Afterwards, we simulated PMG dimensions, namely the spacing between lines, to assess how this parameter would influence electro-optical properties. Theoretically, the larger the spacing, the highest the transmittance and sheet resistance. Simulations performed on COMSOL Multiphysics provided us with sheet resistance values, while optical values for transmittance were taken from Lumerical (FDTD Solver), a software specifically designed for photonics. These simulations gave us an idea of the values we would obtain empirically. When the PMGs were fabricated in the clean room, its electro-optical values did not differ very much from simulations (**Table 5**). Thus, an optimal spacing between lines was found: 22 µm, which allowed us to keep the good electrical properties (6 Ω/sq) while maintaining the optical transparency (81%).

PMG fabrication consisted of basic photolithographic processes using DLW, with the goal of achieving high resolutions (structures a few microns wide). However, high throughput patterning protocols were difficult to attain, discarding gold wet etching from the start because of its unsatisfactory outcomes (**Figure 3.3**), and ending with the lift-off method, whose yield was low, but the samples presented good quality when the method worked (**Figure 3.4**). When we started producing the PMGs in the flexible substrate, Parylene-C, the yield was even lower. A way to work around this problem was to apply an oxygen dry etching pre-treatment before the gold deposition. As such, the oxygen plasma showed to remove PR debris on the unwanted areas, left from the development step, and it also created surface roughness on Parylene-C (**Table 6**) that would later show to be beneficial for the polymer-metal interface. This intermediate step demonstrated to slightly increase sheet resistance (**Figure 3.11**, **Table 7**) and caused the gold to take on a dark color due to optical effects (**Appendix G**). On the other hand, the advantages it offered surpassed these drawbacks. The first advantage is that oxygen plasma greatly improved production yield (**Figure 3.13**), making the final protocol very straightforward and consistent. This occurred because oxygen plasma provided Parylene-C substrate with considerable surface roughness, and the metal-polymer adhesion was improved, increasing the yield during the lift-off process. Finally, in order to determine the liability of the flexible PMG, bending tests were performed, showing approximately zero change in sheet resistance after 1000 bending cycles with 5 mm of bending diameter (**Figure 3.14**).

Afterwards, a 16 electrode ECoG prototype was produced, having each of the electrodes 500 µm distributed over 3 mm of diameter (**Figure 3.15**). The device was later characterized *in vitro* and an impedance magnitude of 13 kΩ at 1 kHz was achieved (**Figure 3.17**), and when compared to the other results in literature, it is one of the lowest values attained to our knowledge (**Table 9**). Results from *in vivo* testing demonstrated that the prototype was able to capture signals with high SNR (**Figure 3.20**). Although electrode transparency is clear, optical imaging measurements are still to be implemented simultaneously with future neural recordings.

Nevertheless, there is always room for improvement, especially when results are dependent on the equipment resolution. By using Nanoimprint Lithography, for instance, it is possible to attain resolutions as high as a few dozens of nanometers. This would help us decrease the linewidth and, consequently, the spacing between the lines, optimizing even more transmittance and sheet resistance values. Moreover, by studying other conductive and biocompatible materials, which may be more easy to pattern than gold, such as titanium nitride, interesting studies can be carried out. Also, adding biocompatible layers, such as polymers on the electrode surface, or embedding molecules in those polymers to minimize inflammation response, would be good for long term brain recordings. Another option to improve the device is to use a two-material configuration, such as a bilayer nanomesh to increase the electrical performance of the device.

In a neuroscientific point of view, it is very interesting to study large areas using a lot of small electrodes. Therefore, to optimize the prototype we could decrease electrode diameter and thus increase the number of electrodes present in the device. However, the more electrodes we have in a device, the more metallic vias need to exist, and they cannot interfere with each other through crosstalk. Hence, we reach a bottleneck where a compromise must exist. To overcome this problem a possible solution is to intercalate metallic vias in different Parylene-C layers.

To further improve neural data acquisition, another approach would be the addition of on-site amplification, such as the incorporation of transistors in the electrodes, to avoid signal loss. Since the limit of Moore's Law is considered to have been achieved, a new class of electronic components are emerging: the memristors. These components can be microfabricated and they are a great alternative to avoid the bottleneck aforementioned. Also, if the basic nanostructure of these memristor electrodes were PMGs, the device would become a really powerful tool.

Concluding, the goal of this work was successfully achieved by producing a transparent, flexible, and low-impedance ECoG device and achieving state-of-the-art results. Furthermore, the main results here presented were published in a poster format (**Appendix J.2**) for the EuroNanoForum2021 virtual conference.

References

[1] J. P. Neto *et al.*, "Transparent and flexible ECoG electrode arrays based on silver nanowire networks for neural recordings," *bioRxiv*, p. 2020.02.24.962878, 2020.

[2] C. Grienberger and A. Konnerth, "Imaging Calcium in Neurons," *Neuron*, vol. 73, no. 5, pp. 862–885, 2012.

[3] N. Kunori and I. Takashima, "A transparent epidural electrode array for use in conjunction with optical imaging," *J. Neurosci. Methods*, vol. 251, pp. 130–137, 2015.

[4] D. Kuzum *et al.*, "Transparent and flexible low noise graphene electrodes for simultaneous electrophysiology and neuroimaging," *Nat. Commun.*, vol. 5, no. May, pp. 1–10, 2014.

[5] M. Thunemann *et al.*, "Deep 2-photon imaging and artifact-free optogenetics through transparent graphene microelectrode arrays," *Nat. Commun.*, vol. 9, no. 1, pp. 1–12, 2018.

[6] H. B. Lee, W. Y. Jin, M. M. Ovhal, N. Kumar, and J. W. Kang, "Flexible transparent conducting electrodes based on metal meshes for organic optoelectronic device applications: A review," *J. Mater. Chem. C*, vol. 7, no. 5, pp. 1087–1110, 2019.

[7] M. G. Guney and G. K. Fedder, "Estimation of line dimensions in 3D direct laser writing lithography," *J. Micromechanics Microengineering*, vol. 26, no. 10, 2016.

[8] E. F. Melcer, M. T. Astolfi, M. Remaley, A. Berenzweig, and T. Giurgica-Tiron, "CTRL-labs: Hand activity estimation and real-time control from neuromuscular signals," *Conf. Hum. Factors Comput. Syst. - Proc.*, vol. 2018-April, pp. 1–4, 2018.

[9] E. Musk, "An integrated brain-machine interface platform with thousands of channels," *bioRxiv*, p. 703801, Jan. 2019.

[10] Z. J. Du *et al.*, "Ultrasoft microwire neural electrodes improve chronic tissue integration," *Acta Biomater.*, vol. 53, pp. 46–58, 2017.

[11] J. M. Rubin, L. L.; Staddon, "The Cell Biology of the Blood-brain barrier," *Annu. Rev. Neurosci.*, vol. 22, no. 1, pp. 11–28, 1999.

[12] T. D. Y. Kozai, A. S. Jaquins-Gerstl, A. L. Vazquez, A. C. Michael, and X. T. Cui, "Brain tissue responses to neural implants impact signal sensitivity and intervention strategies," *ACS Chem. Neurosci.*, vol. 6, no. 1, pp. 48–67, 2015.

[13] R. J. Sadleir and A. Argibay, "Modeling skull electrical properties," *Ann. Biomed. Eng.*, vol. 35, no. 10, pp. 1699–1712, 2007.

[14] E. C. Leuthardt, K. J. Miller, G. Schalk, R. P. N. Rao, and J. G. Ojemann, "Electrocorticography-based brain computer interface - The seattle experience," *IEEE Trans. Neural Syst. Rehabil. Eng.*, vol. 14, no. 2, pp. 194–198, 2006.

[15] M. Fatourechi, A. Bashashati, R. K. Ward, and G. E. Birch, “EMG and EOG artifacts in brain computer interface systems: A survey,” *Clin. Neurophysiol.*, vol. 118, no. 3, pp. 480–494, 2007.

[16] L. F. Nicolas-Alonso and J. Gomez-Gil, “Brain Computer Interfaces, a Review,” *Sensors*, pp. 1211–1279, 2012.

[17] G. Dimitriadis, A. M. M. Fransen, and E. Maris, “Sensory and cognitive neurophysiology in rats. Part 2: Validation and demonstration,” *J. Neurosci. Methods*, vol. 232, pp. 47–57, 2014.

[18] G. Dimitriadis, J. P. Neto, A. Aarts, A. Alexandru, and M. Ballini, “Why not record from every electrode with a CMOS scanning probe ?,” *bioRxiv*, 2020.

[19] G. Dimitriadis, J. P. Neto, and A. R. Kampff, “t-SNE Visualization of Large-Scale Neural Recordings,” vol. 2733, pp. 2709–2733, 2018.

[20] D. Khodagholy *et al.*, “NeuroGrid: recording action potentials from the surface of the brain,” *Nat. Neurosci.*, vol. 18, pp. 310–315, 2014.

[21] T. M. Kandel, Eric R.; Schwartz, James H.; Jessel, “Principles of Neural Science, 4th Edition,” 2000.

[22] J. Eccles, John C.; Ito, Masao; Szentágothai, *The Cerebellum as a Neuronal Machine*, vol. 77, no. 3. 1967.

[23] I. M. Raman and B. P. Bean, “Resurgent sodium current and action potential formation in dissociated cerebellar Purkinje neurons,” *J. Neurosci.*, vol. 17, 1997.

[24] Y. Kajikawa and C. E. Schroeder, “How local is the local field potential?,” *Neuron*, vol. 72, no. 5, pp. 847–858, 2011.

[25] P. L. Nunez and R. Srinivasan, *Electric Fields of the Brain: The neurophysics of EEG*. 2009.

[26] M. Z. Lin and M. J. Schnitzer, “Genetically encoded indicators of neuronal activity,” *Nat. Neurosci.*, vol. 19, no. 9, pp. 1142–1153, 2016.

[27] J. W. T. Thach, “Somatosensory Receptive Fields of Single Units in Cat Cerebellar Cortex,” 1966.

[28] S. Hakimian, S. A. Norris, B. Greger, J. G. Keating, C. H. Anderson, and W. T. Thach, “Time and frequency characteristics of purkinje cell complex spikes in the awake monkey performing a nonperiodic task,” *J. Neurophysiol.*, vol. 100, no. 2, pp. 1032–1040, 2008.

[29] G. Buzsáki, “Large-scale recording of neuronal ensembles,” *Nat. Neurosci.*, vol. 7, no. 5, pp. 446–451, 2004.

[30] J. E. Ramirez and B. M. Stell, “Calcium Imaging Reveals Coordinated Simple Spike Pauses in Populations of Cerebellar Purkinje Cells,” *CellReports*, vol. 17, no. 12, pp. 3125–3132, 2016.

[31] A. S. Machado, D. M. Darmohray, J. Fayad, H. G. Marques, and M. R. Carey, “A quantitative framework for whole-body coordination reveals specific deficits in freely walking ataxic mice,” *Elife*, vol. 4, no. OCTOBER2015, pp. 1–22, 2015.

[32] S. F. Cogan, "Neural Stimulation and Recording Electrodes," *Annu. Rev. Biomed. Eng.*, vol. 10, no. 1, pp. 275–309, 2008.

[33] S. Takeuchi, D. Ziegler, Y. Yoshida, K. Mabuchi, and T. Suzuki, "Parylene flexible neural probes integrated with microfluidic channels," *Lab Chip*, vol. 5, no. 5, pp. 519–523, 2005.

[34] M. R. Fattahi, Pouria; Yang, Guang; Kim, Gloria; Abidian, "A Review of Organic and Inorganic Biomaterials for Nueral Interfaces," *Adv. Mater.*, no. 10, 2014.

[35] X. Wang *et al.*, "Mapping the fine structure of cortical activity with different micro-ECoG electrode array geometries," *J. Neural Eng.*, vol. 14, no. 5, p. aa785e, 2017.

[36] K. J. Seo *et al.*, "Transparent Electrophysiology Microelectrodes and Interconnects from Metal Nanomesh," *ACS Nano*, vol. 11, no. 4, pp. 4365–4372, 2017.

[37] Z. Chen *et al.*, "Flexible and Transparent Metal Oxide/Metal Grid Hybrid Interfaces for Electrophysiology and Optogenetics," *Adv. Mater. Technol.*, vol. 5, no. 8, pp. 1–8, 2020.

[38] T. Ryynänen *et al.*, "Microelectrode Array With Transparent ALD TiN Electrodes," *Front. Neurosci.*, vol. 13, no. March, pp. 1–7, 2019.

[39] J. Neto *et al.*, "Transparent and flexible ECoG electrode arrays based on silver nanowire networks for neural recordings," 2020. .

[40] P. Ledochowitsch *et al.*, "Strategies for optical control and simultaneous electrical readout of extended cortical circuits," *J. Neurosci. Methods*, vol. 256, pp. 220–231, 2015.

[41] J. H. Park *et al.*, "Flexible and transparent metallic grid electrodes prepared by evaporative assembly," *ACS Appl. Mater. Interfaces*, vol. 6, no. 15, pp. 12380–12387, 2014.

[42] M. R. Abidian, K. A. Ludwig, T. C. Marzullo, D. C. Martin, and D. R. Kipke, "Interfacing conducting polymer nanotubes with the central nervous system: chronic neural recording using poly(3,4-ethylenedioxythiophene) nanotubes," *Adv. Mater.*, vol. 21, no. 37, pp. 3764–3770, 2009.

[43] D. Khodagholy *et al.*, "Highly conformable conducting polymer electrodes for in vivo recordings," *Adv. Mater.*, vol. 23, no. 36, pp. 268–272, 2011.

[44] A. Susloparova *et al.*, "Low impedance and highly transparent microelectrode arrays (MEA) for in vitro neuron electrical activity probing," *Sensors Actuators, B Chem.*, vol. 327, no. September 2020, 2021.

[45] P. P. Edwards, A. Porch, M. O. Jones, D. V. Morgan, and R. M. Perks, "Basic materials physics of transparent conducting oxides," *Dalt. Trans.*, no. 19, pp. 2995–3002, 2004.

[46] T. D. Y. Kozai and A. L. Vazquez, "Photoelectric artefact from optogenetics and imaging on microelectrodes and bioelectronics: new challenges and opportunities," *J. Mater. Chem. B*, vol. 3, no. 25, pp. 4965–4978, 2015.

[47] S. Sharma, S. Shriwastava, S. Kumar, K. Bhatt, and C. C. Tripathi, "Alternative transparent conducting

electrode materials for flexible optoelectronic devices," *Opto-electronics Rev.*, vol. 26, no. 3, pp. 223–235, 2018.

[48] Y. Liu, Y. Zhao, B. Sun, and C. Chen, "Understanding the toxicity of carbon nanotubes," *Acc. Chem. Res.*, vol. 46, no. 3, pp. 702–713, 2013.

[49] D. S. Hecht, L. Hu, and G. Irvin, "Emerging transparent electrodes based on thin films of carbon nanotubes, graphene, and metallic nanostructures," *Adv. Mater.*, vol. 23, no. 13, pp. 1482–1513, 2011.

[50] A. R. Harris, S. J. Morgan, J. Chen, R. M. I. Kapsa, G. G. Wallace, and A. G. Paolini, "Conducting polymer coated neural recording electrodes," *J. Neural Eng.*, vol. 10, no. 1, 2013.

[51] R. A. Green, N. H. Lovell, G. G. Wallace, and L. A. Poole-Warren, "Conducting polymers for neural interfaces: Challenges in developing an effective long-term implant," *Biomaterials*, vol. 29, no. 24–25, pp. 3393–3399, 2008.

[52] J. Y. Lee, S. T. Connor, Y. Cui, and P. Peumans, "Solution-processed metal nanowire mesh transparent electrodes," *Nano Lett.*, vol. 8, no. 2, pp. 689–692, 2008.

[53] J. L. Elechiguerra, L. Larios-Lopez, C. Liu, D. Garcia-Gutierrez, A. Camacho-Bragado, and M. J. Yacaman, "Corrosion at the nanoscale: The case of silver nanowires and nanoparticles," *Chem. Mater.*, vol. 17, no. 24, pp. 6042–6052, 2005.

[54] J. Schneider, P. Rohner, D. Thureja, M. Schmid, P. Galliker, and D. Poulikakos, "Electrohydrodynamic NanoDrip Printing of High Aspect Ratio Metal Grid Transparent Electrodes," *Adv. Funct. Mater.*, vol. 26, no. 6, pp. 833–840, 2016.

[55] S. Hong *et al.*, "Nonvacuum, Maskless Fabrication of a Flexible Metal Grid Transparent Conductor by Low-Temperature Selective Laser Sintering of Nanoparticle Ink," *ACS Nano*, no. Xx, 2013.

[56] X. Chen *et al.*, "Embedded Ag/Ni Metal-Mesh with Low Surface Roughness As Transparent Conductive Electrode for Optoelectronic Applications," *ACS Appl. Mater. Interfaces*, vol. 9, no. 42, pp. 37048–37054, 2017.

[57] A. J. Morfa, E. M. Akinoglu, J. Subbiah, M. Giersig, and P. Mulvaney, "Transparent metal electrodes from ordered nanosphere arrays," *J. Appl. Phys.*, vol. 114, no. 5, 2013.

[58] Y. Qiang *et al.*, "Bilayer Nanomesh Structures for Transparent Recording and Stimulating Microelectrodes," *Adv. Funct. Mater.*, vol. 27, no. 48, pp. 1–12, 2017.

[59] Y. Qiang *et al.*, "Transparent arrays of bilayer-nanomesh microelectrodes for simultaneous electrophysiology and two-photon imaging in the brain," *Sci. Adv.*, vol. 4, no. 9, 2018.

[60] D. Lordan *et al.*, "Asymmetric Pentagonal Metal Meshes for Flexible Transparent Electrodes and Heaters," *ACS Appl. Mater. Interfaces*, vol. 9, no. 5, pp. 4932–4940, 2017.

[61] G. Torrisi *et al.*, "Colloidal-structured metallic micro-grids: High performance transparent electrodes

in the red and infrared range," *Sol. Energy Mater. Sol. Cells*, vol. 197, pp. 7–12, 2019.

[62] J. P. Neto, "JoanaPNeto - GitHub." [Online]. Available: https://github.com/JoanaPNeto. [Accessed: 28-Apr-2021].

[63] G. Seguini, J. Llamoja Curi, S. Spiga, G. Tallarida, C. Wiemer, and M. Perego, "Solid-state dewetting of ultra-thin Au films on SiO2and HfO2," *Nanotechnology*, vol. 25, no. 49, 2014.

[64] D. Meyerhofer, "proximity effect effect in optical optical lithography lithography Resolution and proximity The question," vol. 922, pp. 174–187, 1988.

[65] S. Q. Hussain *et al.*, "RF magnetron sputtered ITO:Zr thin films for the high efficiency a-Si:H/c-Si heterojunction solar cells," *Met. Mater. Int.*, vol. 20, no. 3, pp. 565–569, 2014.

[66] K. Leosson, A. S. Ingason, B. Agnarsson, A. Kossoy, S. Olafsson, and M. C. Gather, "Ultra-thin gold films on transparent polymers," *Nanophotonics*, vol. 2, no. 1, pp. 3–11, 2013.

[67] "Gold - RRUFF Database: Raman, X-ray, Infrared, and Chemistry." [Online]. Available: https://rruff.info/Gold. [Accessed: 28-Apr-2021].

[68] R. Seghir and S. Arscott, "Controlled mud-crack patterning and self-organized cracking of polydimethylsiloxane elastomer surfaces," *Sci. Rep.*, vol. 5, no. October, pp. 1–16, 2015.

[69] M. E. P. Tweedie, C. S. Lau, L. Hou, X. Wang, Y. Sheng, and J. H. Warner, "Transparent ultrathin all-two-dimensional lateral Gr:WS2:Gr photodetector arrays on flexible substrates and their strain induced failure mechanisms," *Mater. Today Adv.*, vol. 6, p. 100067, 2020.

[70] H. Marom and M. Eizenberg, "The effect of surface roughness on the resistivity increase in nanometric dimensions," *J. Appl. Phys.*, vol. 99, no. 12, pp. 1–8, 2006.

[71] Y. Lu *et al.*, "Ultralow Impedance Graphene Microelectrodes with High Optical Transparency for Simultaneous Deep Two-Photon Imaging in Transgenic Mice," *Adv. Funct. Mater.*, vol. 28, no. 31, pp. 1–9, 2018.

[72] J. Zhang *et al.*, "Stretchable Transparent Electrode Arrays for Simultaneous Electrical and Optical Interrogation of Neural Circuits in Vivo," *Nano Lett.*, vol. 18, no. 5, pp. 2903–2911, 2018.

[73] T. Ryynänen *et al.*, "Microelectrode array for noninvasive analysis of cardiomyocytes at the single-cell level," *Jpn. J. Appl. Phys.*, vol. 57, no. 11, pp. 1–7, 2018.

[74] J. W. Seo *et al.*, "Artifact-Free 2D Mapping of Neural Activity In Vivo through Transparent Gold Nanonetwork Array," *Adv. Funct. Mater.*, vol. 30, no. 34, pp. 1–11, 2020.

[75] J. W. Lim *et al.*, "Effect of geometric lattice design on optical/electrical properties of transparent silver grid for organic solar cells," *Opt. Express*, vol. 22, no. 22, p. 26891, 2014.

[76] W. Kim *et al.*, "Hybrid Silver Mesh Electrode for ITO-Free Flexible Polymer Solar Cells with Good Mechanical Stability," *ChemSusChem*, vol. 9, no. 9, pp. 1042–1049, 2016.

[77] D. Lordan, “Alternative materials for flexible transparent conductive electrodes,” University College Cork, 2017.

[78] S. Varagnolo, K. W. Park, J. K. Lee, and R. A. Hatton, “Embedded-grid silver transparent electrodes fabricated by selective metal condensation,” *J. Mater. Chem. C*, vol. 8, no. 38, pp. 13453–13457, 2020.

[79] M. G. Kang and L. J. Guo, “Nanoimprinted semitransparent metal electrodes and their application in organic light-emitting diodes,” *Adv. Mater.*, vol. 19, no. 10, pp. 1391–1396, 2007.

[80] J. Linnet, A. R. Walther, C. Wolff, O. Albrektsen, N. A. Mortensen, and J. Kjelstrup-Hansen, “Transparent and conductive electrodes by large-scale nano-structuring of noble metal thin-films,” *Opt. Mater. Express*, vol. 8, no. 7, p. 1733, 2018.

[81] T. Nakanishi *et al.*, “Electrical resistivity of transparent metal nanomesh electrodes,” *Phys. Status Solidi Appl. Mater. Sci.*, vol. 210, no. 2, pp. 327–334, 2013.

[82] M. Layani, R. Berman, and S. Magdassi, “Printing holes by a dewetting solution enables formation of a transparent conductive film,” *ACS Appl. Mater. Interfaces*, vol. 6, no. 21, pp. 18668–18672, 2014.

[83] Y. Liu, S. Shen, J. Hu, and L. Chen, “Embedded Ag mesh electrodes for polymer dispersed liquid crystal devices on flexible substrate,” *Opt. Express*, vol. 24, no. 22, p. 25774, 2016.

[84] G. Burwell *et al.*, “Metal Grid Structures for Enhancing the Stability and Performance of Solution-Processed Organic Light-Emitting Diodes,” *Adv. Electron. Mater.*, vol. 6, no. 12, 2020.

[85] M. Pereira *et al.*, “Noble-Metal-Free Memristive Devices Based on IGZO for Neuromorphic Applications,” *Adv. Electron. Mater.*, vol. 6, no. 10, pp. 1–9, 2020.

Appendices

Appendix A – Overview of PMG materials, fabrication techniques, dimensions, and results for different geometries

The following tables present a detailed analysis regarding the state-of-the-art PMG materials, fabrication techniques, dimensions (linewidth, pitch and thickness), and results (sheet resistance R_S, transmittance T at 550 nm, and Figure of Merit (FOM)) for different geometries, namely square and rectangular grids, circular shapes, honeycomb structures, triangular shapes, and asymmetric grids (pentagonal). For the sake of comparison, for a thickness of 80 nm of ITO the R_S is 70 Ω/sq and the transmittance is 82 % at 550 nm [65].

Table A.1 – Square PMG.

Reference	Material	Technique	Linewidth	Pitch	Thickness	R_S (Ω/sq)	T (%)	FOM
[75]	Ag	Photolithography	5 µm	100 µm	50 nm	13.27	81.1	129.05
				50 µm		6.61	72.7	164.61
	Ag	Roll-to-roll process	6 µm	220 µm	50-75 µm	15-30	85	-
[76]	Ag/PEDOT	Printing	60 µm	1000 µm	3 µm	16.50	80	-
[54]	Ag	NanoDrip	500 nm	20 µm		58	98	-
	Au					8	94	-
[55]	Ag NPs	Selective laser sintering	12 µm	300 µm		30	85	-
[77]	Cu	UV Lithography				6.5	75	261
	Ni					28	76.5	65
	Pt					3	74	532
	Al	Nanoimprint Lithography				13	75	131
	Cu					22	78	94
	Au					12		87

	Ag	Rolling Mask Lithography				5	89	1828
	Al					3.5	89	2612
[78]	Ag	Selective metal condensation	1.7 µm	24.2 µm	90 nm	20	88	-
[37]	Au/ITO	UV Lithography	10 µm	80 µm	80 nm	5.6	59	-
			3 µm	90 µm	80 nm	14.1	81	-

Table A.2 – Rectangular PMG.

Reference	Material	Technique	Linewidth	Pitch	Thickness (nm)	R_S (Ω/sq)	T (%)
[79]	Cu	Nanoimprint Lithography	120 nm	700 nm	40	15	73
					60	8	70
					80	5	65
	Au				40	12	74
					60	7	65
					80	5	60
	Al				40	13	75
					60	8	65
					80	5	65

Table A.3 – Circular PMG.

Reference	Material	Technique	Sphere Diameter	Thickness	R_S (Ω/sq)	|Z|	T (%)
[61]	Ag	Colloidal lithography	16 µm	17 nm	12.8	-	72
			5 µm	17 nm	126	-	70
[80]	Al	Simulation	400 µm	20 nm	15	-	85
	Ti+Ag	Colloidal lithography	1 µm	33 nm	10	-	80
	Ag	Colloidal lithography	1.6 µm	20 nm	10.6	-	75
			5 µm	10 nm	121	-	85
[58]	Au/IrO	Colloidal lithography	1 µm	15 nm	-	30	70
[59]	Au/PEDOT	Colloidal lithography	1 µm	25 nm	-	130	70
[36]	Au	Nanosphere lithography	1 µm	15 nm	-	127.2	65
[57]	Ag	Nanosphere lithography	756 nm	50 nm	3	-	73
[81]	Ag	Nanoimprint Lithography	38.8 nm	40 nm	1.88	-	45
	Au		42 nm		2.12	-	
[82]	Ag NPs	Inkjet printing/ Sel Assembly	80 µm	200 nm	9	-	80

Table A.4 – Honeycomb PMG.

Reference	Material	Technique	Linewidth	Side Length	Thickness	R_S (Ω/sq)	T (%)	FOM
[77]	Au	Photolithography				14	59	48
[56]	Ag/Ni	Printing/ Electroplating	24 µm	70 µm	3 µm	2.1	88.6	1450
[83]	Ag	DLW	3 µm	150 µm	2.5 µm	3.5	92	-
[84]	Ni/Ag/Al	Photolithography	20 µm	1 mm	1 µm	<1	-	-

Table A.5 – Triangular PMG.

Reference	Material	Technique	Linewidth	Thickness	R_S (Ω/sq)	T (%)	FOM
[75]	Ag	Photolithography/ Sputtering	5 µm	50 nm	7.07	74.9	171.14
			24 µm	3 µm	7.75	76.6	170.18

Table A.6 – Asymmetric PMG (pentagonal).

Reference	Material	Technique	Linewidth	Thickness	R_S (Ω/sq)	T (%)	FOM
[60]	Pt	E-Beam			27.83	78	

Appendix B – Accessory used for transmittance measurements

It was necessary to produce an accessory to carry out the transmittance measurements. It worked not only as a holder for the sample, which was attached with tape, but it also limited the light passing through, since the circular hole and the part of the sample we want to analyze had approximately the same area (~ 2 mm of diameter). The accessory was designed in Adobe Illustrator®. Using a Laser System VLS3.50: Cutting and Engraving Machine it was possible to cut an acrylic plaque and tailor it into the accessory very easily and rapidly. After the laser cutting, it was covered with black adhesive paper so it would not interfere with the transmittance analysis.

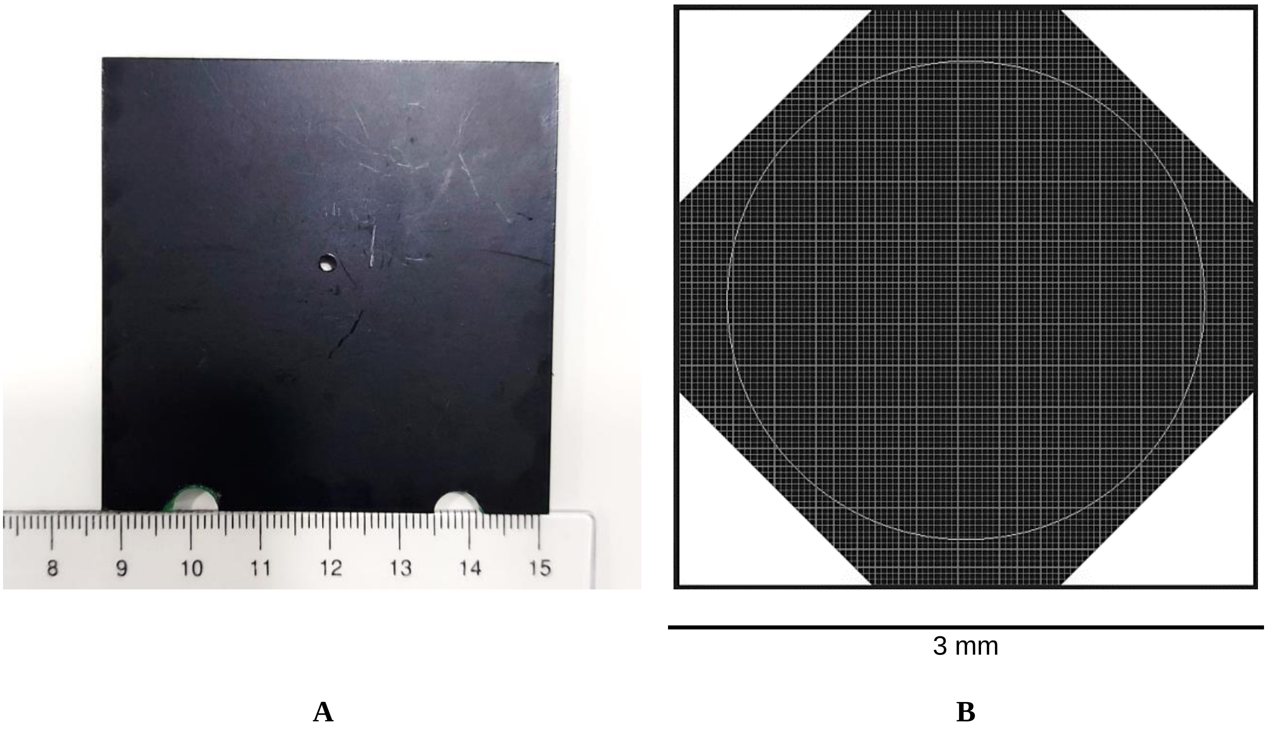

Figure B.1 – A) Accessory for transmittance measurements; B) Schematic of PMG design with the four contacts for Hall measurements (each contact has 1 mm on the side), and with the limited circular area for transmittance analysis (2 mm of diameter), having the whole design in total 3 mm^2.

Appendix C – Encapsulation Photolithography Mask Fabrication Process

The mask to protect Parylene-C encapsulation layer from being etched was fabricated on a glass substrate, previously cleaned in ultrasonic baths of acetone and isopropanol, then rinsed with DI-water and blow dried with nitrogen spray gun. Mask material consists of a 300 nm thick molybdenum layer deposited by RF magnetron sputtering in an AJA ATC-1800 system with a flow rate of 50 sccm of Argon, a sputtering power of 175 W, and a deposition pressure of 1.7 mTorr. Afterwards, negative photoresist (AZ® nLOF 2020 from MicroChemicals GmbH) was deposited through spin-coating at 3000 rpm for 30 s, then soft-baked at 110 ºC for 2 min. The exposure step was made in DLW with exposure conditions of 15 mW at 60 % with filter using the 2 µm head, according to the image depicted in **Figure C.1**, previously designed in KLayout software. After the post-exposure bake for 2 min also at 110 ºC, the sample was developed in AZ® 726 MIF (MicroChemicals GmbH) then immersed in DI-water bath and dried with N_2 spray gun. The pattering was achieved by RIE in a Trion Phantom 3 system, using SF_6 and according to the conditions of 50 W of RF power, 10 sccm of flux, 50 mTorr of pressure, 25 ºC of temperature, and for 5 to 10 min of duration. [85]

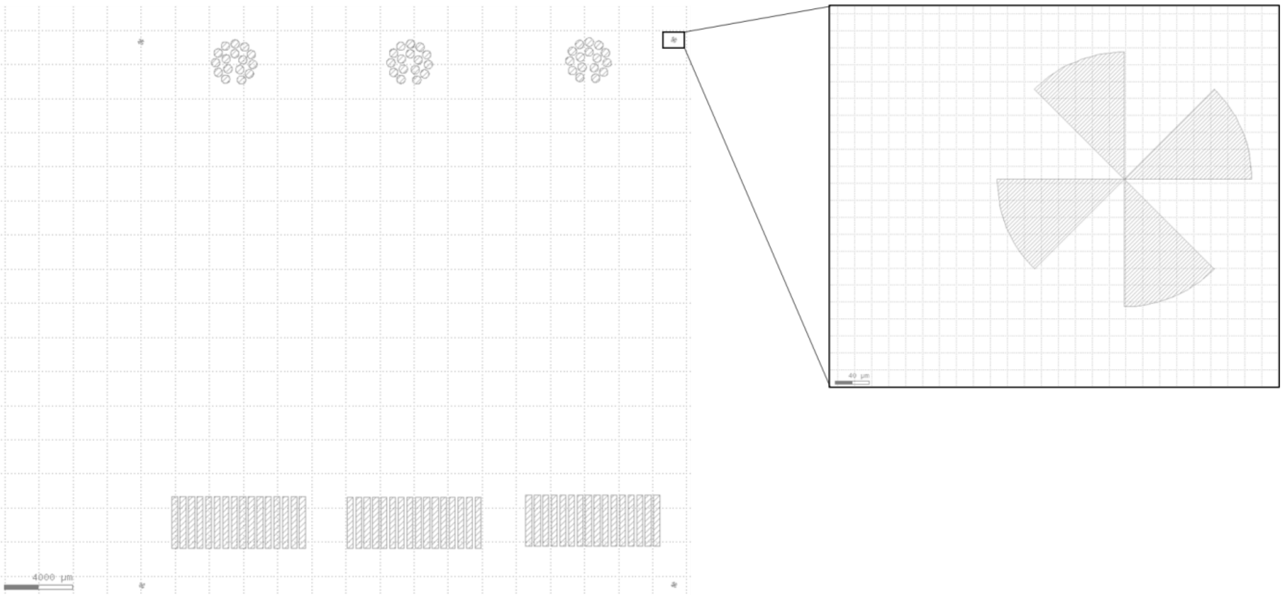

Figure C.1 – Encapsulation mask designed in KLayout. We can observe the alignment marks in the corners, as well as the circles to cover the electrodes and the rectangles below to cover the connection pads.

Appendix D – Wet Etching Protocol and Setup

Samples for the wet etching tests were fabricated on glass substrates previously cleaned in subsequent ultrasonic baths of acetone and isopropanol, followed by rinsing with DI-water and dried with nitrogen spray gun. The gold was then deposited as described in Chapter 3 for the PMGs and ECoG prototype. Afterwards, negative photoresist was spin-coated, soft-baked, and the exposure was according to the illustration depicted in **Figure 3.2**. After the development, an oxygen plasma treatment of 10 min was performed, as suggested by the gold etchant manufacturer, to remove organic residues and improve gold wet etching. The setup for wet etching can be seen in **Figure D.1**, where the etchant recipient, with the sample immersed, is in an oil bath to keep a constant temperature of 80 ºC. The optimal time for this process was studied and, for analysis, the samples were cleaned with isopropanol, rinsed with DI-water and dried with N_2.

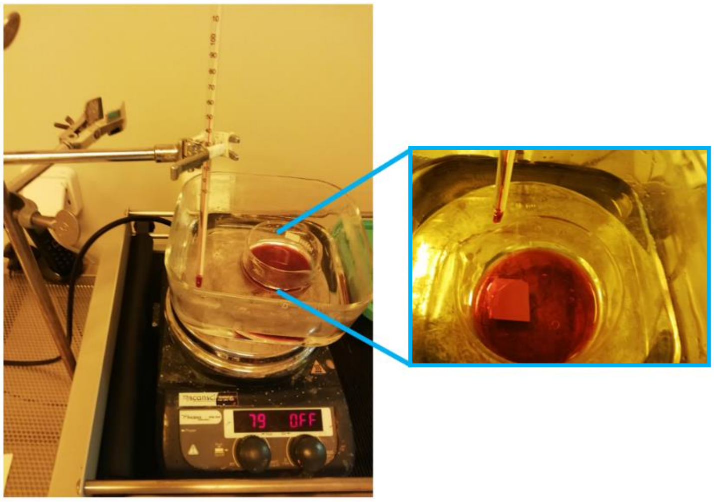

Figure D.1 – Gold wet etching setup.

Appendix E – Profilometry measurement of E-Beam PVD of gold

In order to assess how the thickness of the gold deposition is distributed in the electron-beam system, twelve silicon substrates were placed all over the substrate holder according to **Figure E.1**, and the gold thickness was then measured in the profilometer. The presumed thickness is 6 nm of titanium (adhesion layer) and 80 nm of gold, which sums up to 86 nm. The average thickness attained was 88 ± 7.4 nm, which does not diverge very much from the assumed thickness of 86 nm. Nevertheless, the maximum difference was 22 nm which may cause variability in the wet etching process.

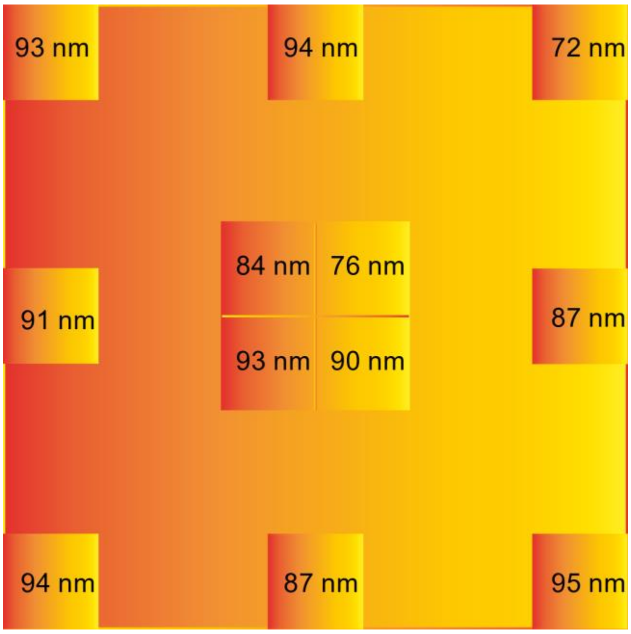

Figure E.1 – Measured Ti/Au thickness in the different quadrants of the E-Beam substrate holder platform.

Appendix F – Gold PMG SEM Images

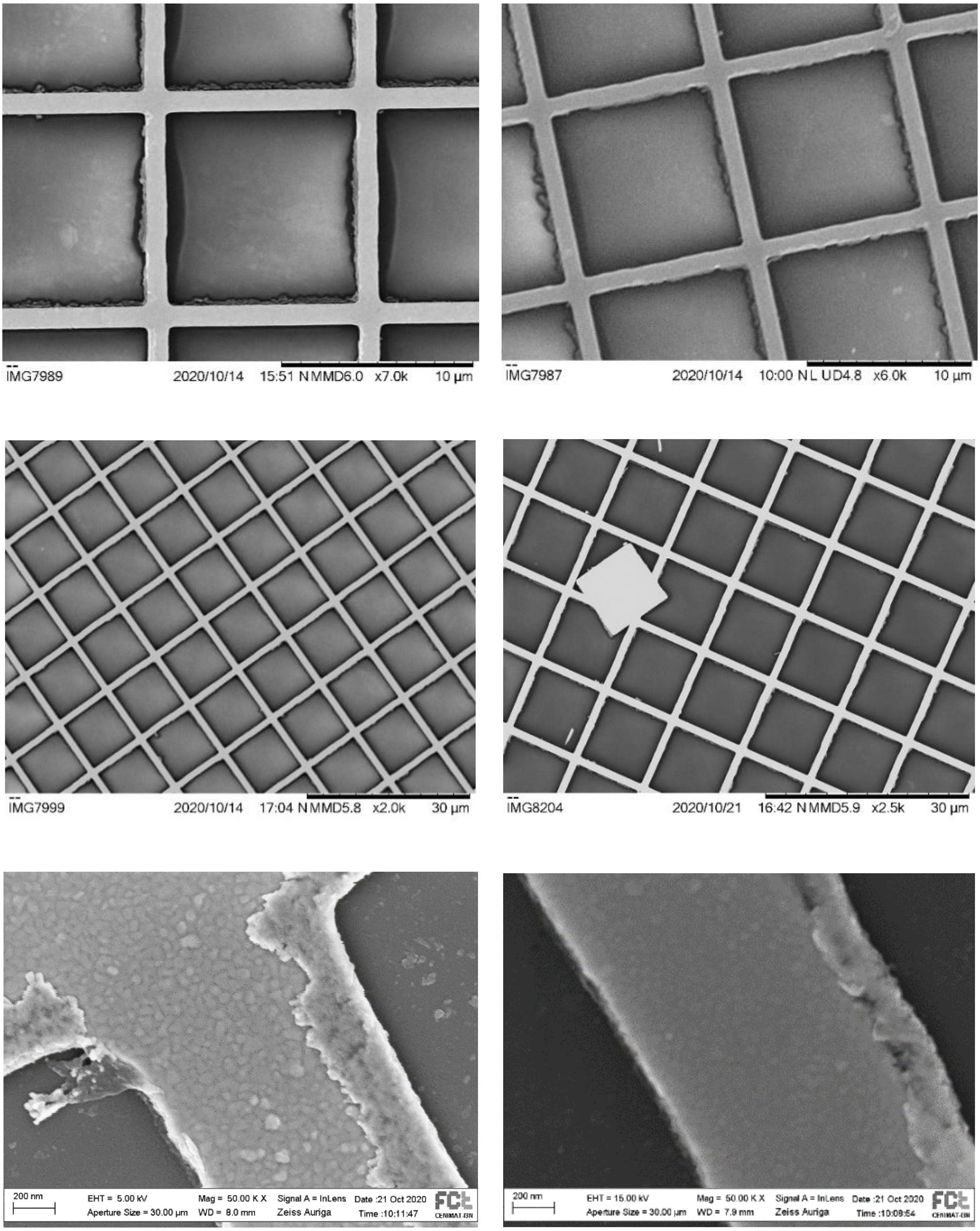

Figure F.1 – SEM images of the gold PMGs.

Appendix G – Oxygen dry etching effect on gold color

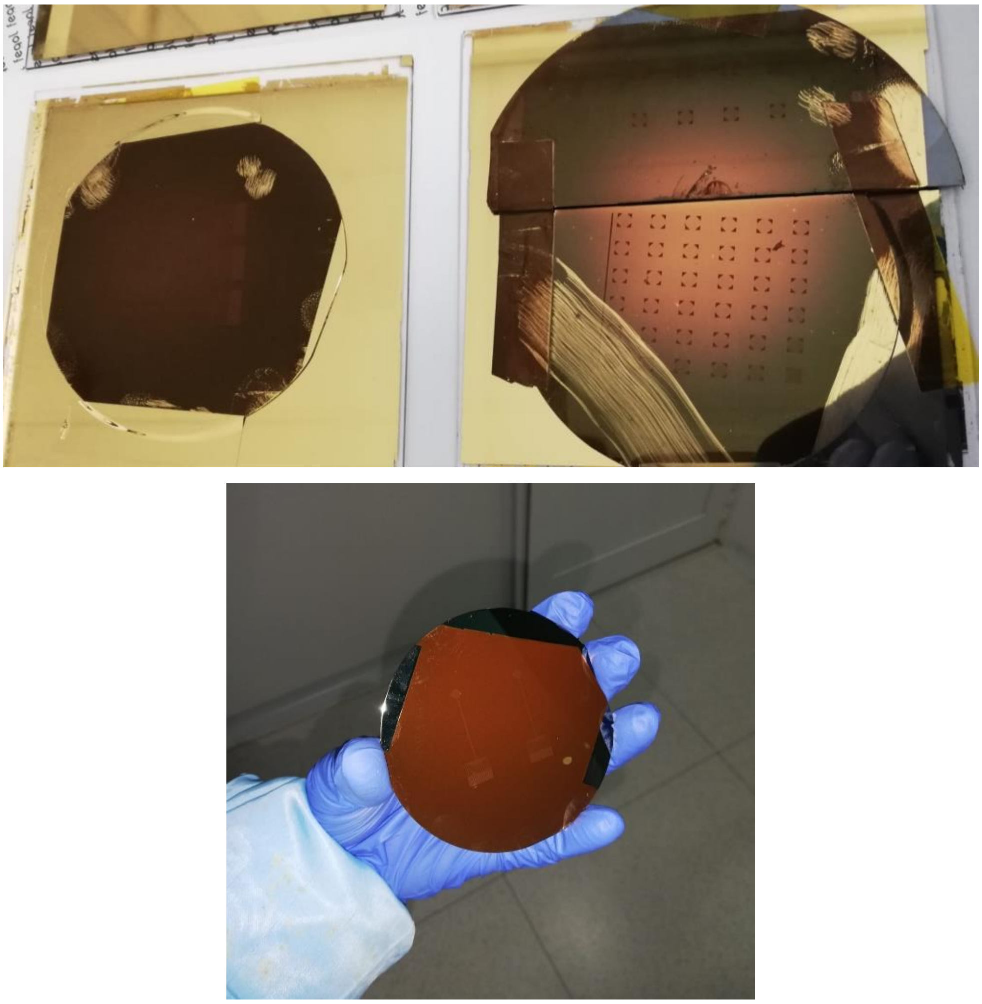

Figure G.1 – ECoG prototypes and PMGs with gold color affected by the oxygen dry etching pre-treatment.

Appendix H – Control Devices

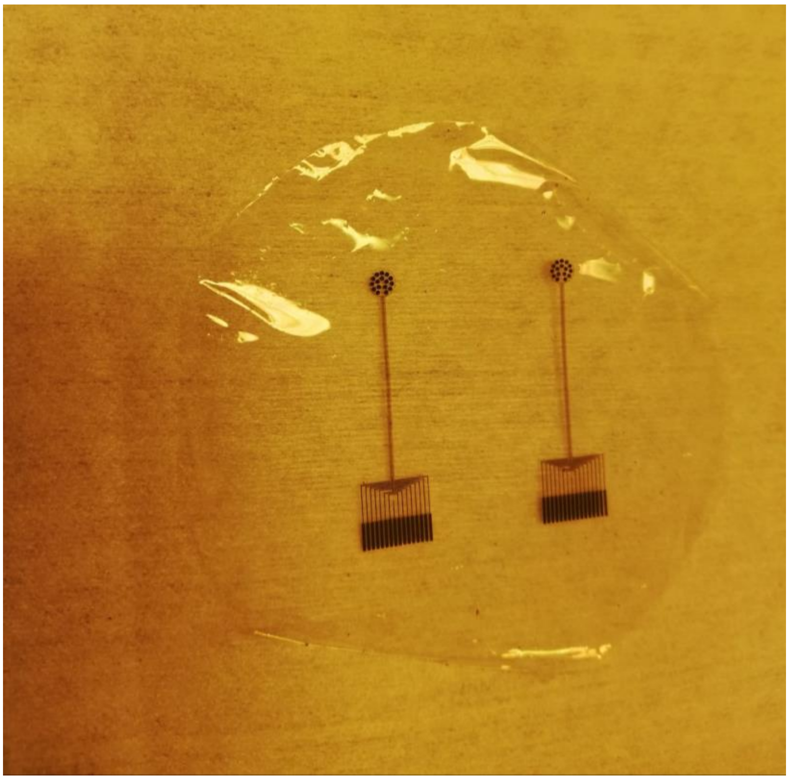

Figure H.1 – Control devices.

Appendix I – Pictures taken during surgery

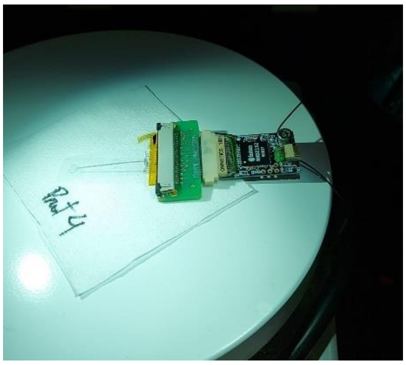

Figure I.1 – ECoG prototype assembled with the ZIF adapter.

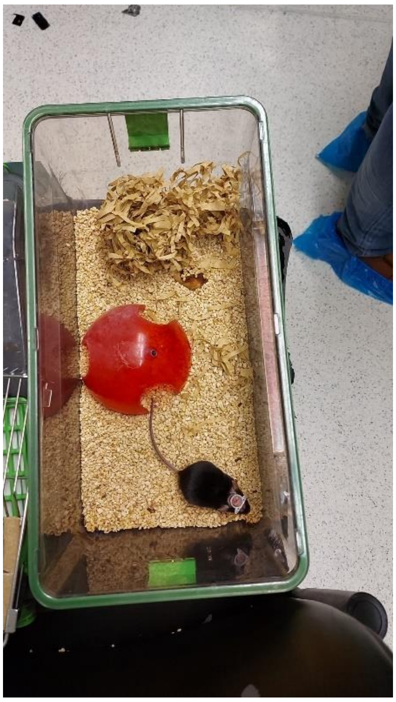

Figure I.2 – Mouse in its cage already with the headbar and cranial window.

Appendix J – Other works related to the master thesis project

Appendix J.1

Class given in the scope of “Nanofabrication and Nanostructures Characterization” course regarding maskless photolithography production using DLW.

https://drive.google.com/file/d/1INCUuN_cf5KPEtM3USoK7mP07DD2VU24/view

Final questionnaire:

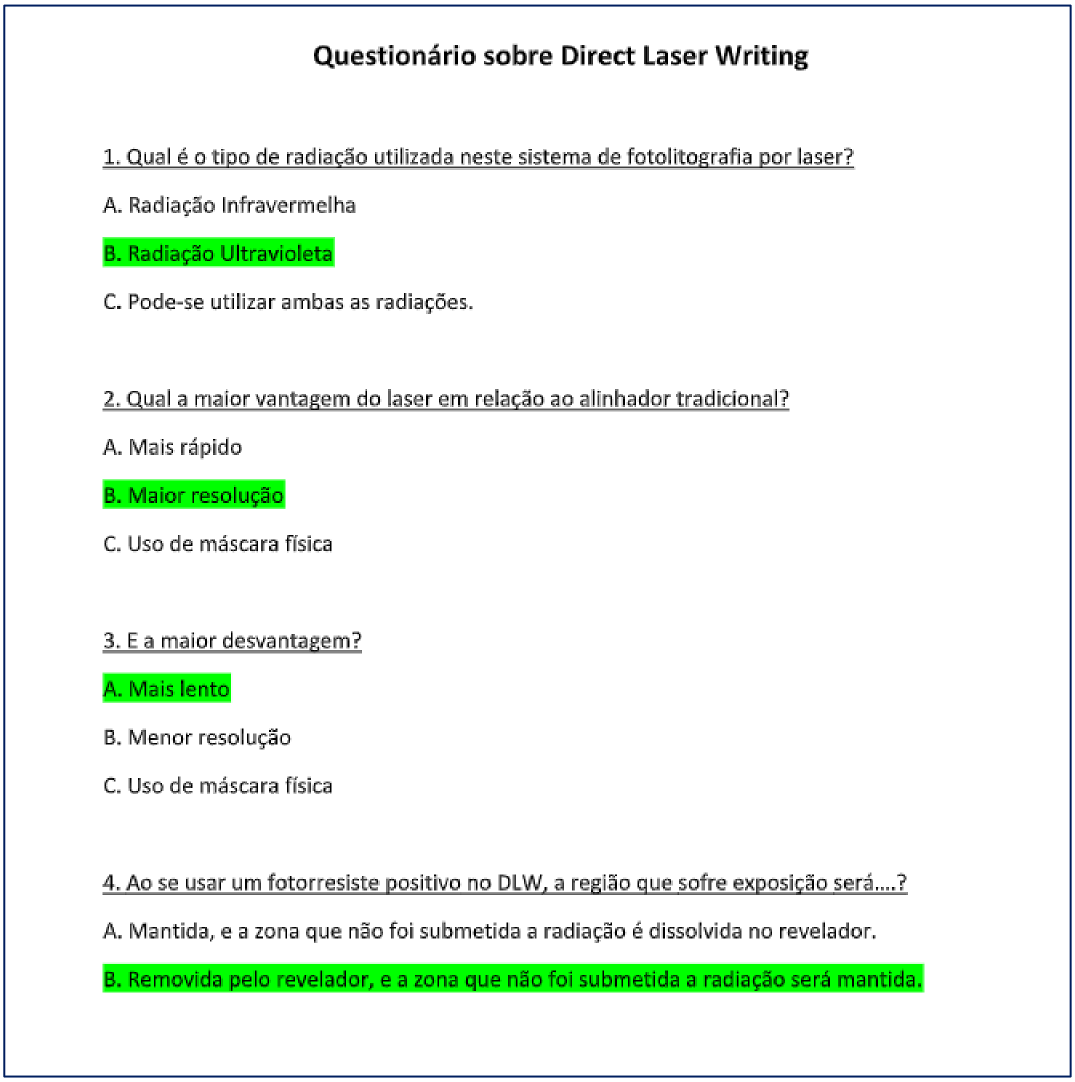

Questionário sobre Direct Laser Writing

1. Qual é o tipo de radiação utilizada neste sistema de fotolitografia por laser?

A. Radiação Infravermelha

B. Radiação Ultravioleta

C. Pode-se utilizar ambas as radiações.

2. Qual a maior vantagem do laser em relação ao alinhador tradicional?

A. Mais rápido

B. Maior resolução

C. Uso de máscara física

3. E a maior desvantagem?

A. Mais lento

B. Menor resolução

C. Uso de máscara física

4. Ao se usar um fotorresiste positivo no DLW, a região que sofre exposição será….?

A. Mantida, e a zona que não foi submetida a radiação é dissolvida no revelador.

B. Removida pelo revelador, e a zona que não foi submetida a radiação será mantida.

Appendix J.2

Scientific poster for exhibition in the EuroNanoForum 2021 virtual conference organized by INL – International Iberian Nanotechnology Laboratory.

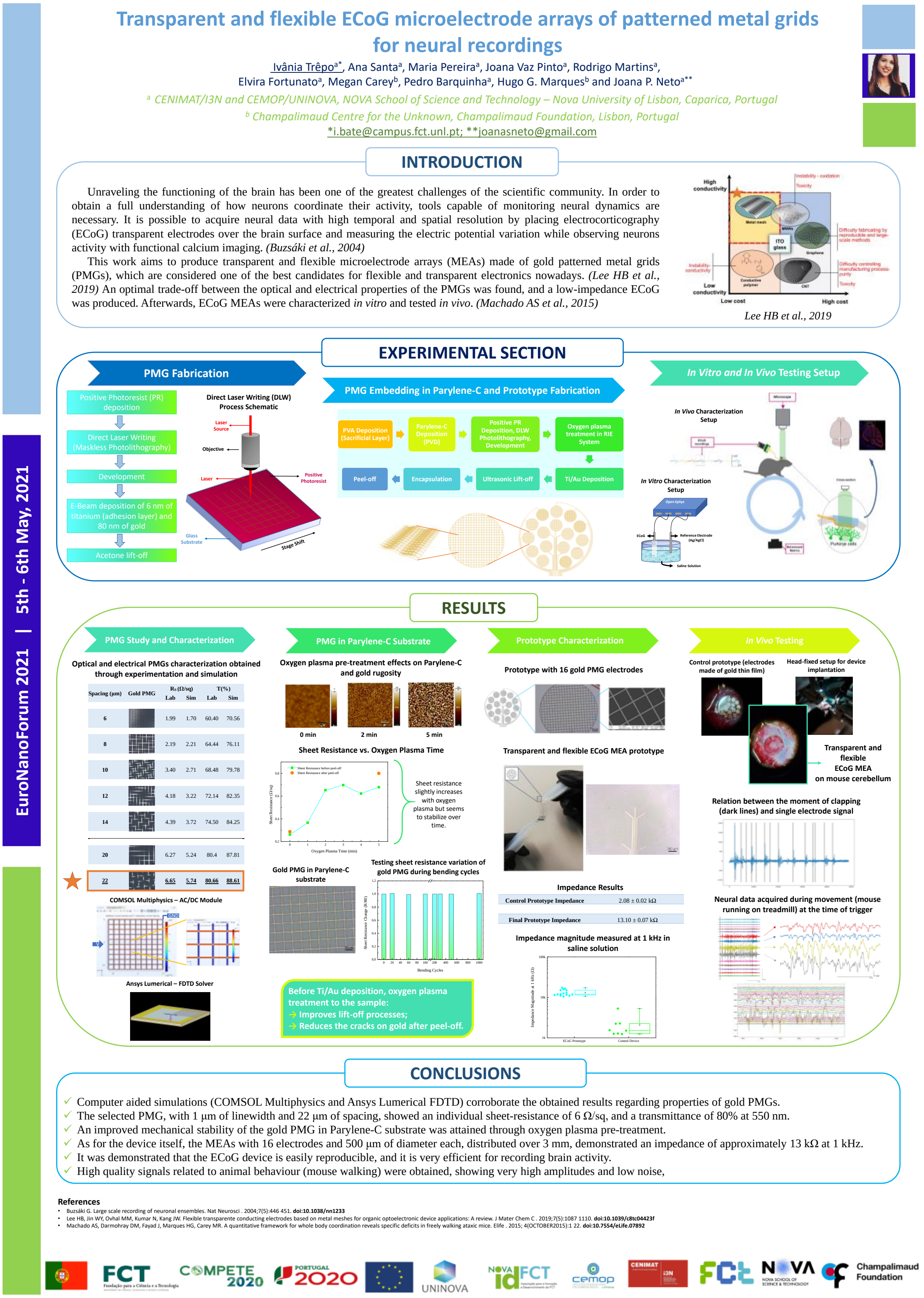

EuroNanoForum 2021 | 5th - 6th May, 2021

Transparent and flexible ECoG microelectrode arrays of patterned metal grids for neural recordings

Ivânia Trêpo[a*], Ana Santa[a], Maria Pereira[a], Joana Vaz Pinto[a], Rodrigo Martins[a],
Elvira Fortunato[a], Megan Carey[b], Pedro Barquinha[a], Hugo G. Marques[b] and Joana P. Neto[a**]

[a] CENIMAT/I3N and CEMOP/UNINOVA, NOVA School of Science and Technology – Nova University of Lisbon, Caparica, Portugal
[b] Champalimaud Centre for the Unknown, Champalimaud Foundation, Lisbon, Portugal
*i.bate@campus.fct.unl.pt; **joanasneto@gmail.com

INTRODUCTION

Unraveling the functioning of the brain has been one of the greatest challenges of the scientific community. In order to obtain a full understanding of how neurons coordinate their activity, tools capable of monitoring neural dynamics are necessary. It is possible to acquire neural data with high temporal and spatial resolution by placing electrocorticography (ECoG) transparent electrodes over the brain surface and measuring the electric potential variation while observing neurons activity with functional calcium imaging. *(Buzsáki et al., 2004)*

This work aims to produce transparent and flexible microelectrode arrays (MEAs) made of gold patterned metal grids (PMGs), which are considered one of the best candidates for flexible and transparent electronics nowadays. *(Lee HB et al., 2019)* An optimal trade-off between the optical and electrical properties of the PMGs was found, and a low-impedance ECoG was produced. Afterwards, ECoG MEAs were characterized *in vitro* and tested *in vivo*. *(Machado AS et al., 2015)*

Lee HB et al., 2019

EXPERIMENTAL SECTION

PMG Fabrication

Positive Photoresist (PR) deposition
Direct Laser Writing (Maskless Photolithography)
Development
E-Beam deposition of 6 nm of titanium (adhesion layer) and 80 nm of gold
Acetone lift-off

Direct Laser Writing (DLW) Process Schematic

PMG Embedding in Parylene-C and Prototype Fabrication

PVA Deposition (Sacrificial Layer) → Parylene-C Deposition (PVD) → Positive PR Deposition, DLW Photolithography, Development → Oxygen plasma treatment in RIE System → Ti/Au Deposition → Ultrasonic Lift-off → Encapsulation → Peel-off

In Vitro and In Vivo Testing Setup

In Vivo Characterization Setup

In Vitro Characterization Setup

RESULTS

PMG Study and Characterization

Optical and electrical PMGs characterization obtained through experimentation and simulation

Spacing (μm)	Gold PMG	R_S (Ω/sq) Lab	R_S (Ω/sq) Sim	T(%) Lab	T(%) Sim
6		1.99	1.70	60.40	70.56
8		2.19	2.21	64.44	76.11
10		3.40	2.71	68.48	79.78
12		4.18	3.22	72.14	82.35
14		4.39	3.72	74.50	84.25
20		6.27	5.24	80.4	87.81
22		**6.65**	**5.74**	**80.66**	**88.61**

COMSOL Multiphysics – AC/DC Module

Ansys Lumerical – FDTD Solver

PMG in Parylene-C Substrate

Oxygen plasma pre-treatment effects on Parylene-C and gold rugosity

0 min 2 min 5 min

Sheet Resistance vs. Oxygen Plasma Time

Sheet resistance slightly increases with oxygen plasma but seems to stabilize over time.

Gold PMG in Parylene-C substrate

Testing sheet resistance variation of gold PMG during bending cycles

Before Ti/Au deposition, oxygen plasma treatment to the sample:
→ Improves lift-off processes;
→ Reduces the cracks on gold after peel-off.

Prototype Characterization

Prototype with 16 gold PMG electrodes

Transparent and flexible ECoG MEA prototype

Impedance Results

Control Prototype Impedance	2.08 ± 0.02 kΩ
Final Prototype Impedance	13.10 ± 0.07 kΩ

Impedance magnitude measured at 1 kHz in saline solution

In Vivo Testing

Control prototype (electrodes made of gold thin film)

Head-fixed setup for device implantation

Transparent and flexible ECoG MEA on mouse cerebellum

Relation between the moment of clapping (dark lines) and single electrode signal

Neural data acquired during movement (mouse running on treadmill) at the time of trigger

CONCLUSIONS

- ✓ Computer aided simulations (COMSOL Multiphysics and Ansys Lumerical FDTD) corroborate the obtained results regarding properties of gold PMGs.
- ✓ The selected PMG, with 1 μm of linewidth and 22 μm of spacing, showed an individual sheet-resistance of 6 Ω/sq, and a transmittance of 80% at 550 nm.
- ✓ An improved mechanical stability of the gold PMG in Parylene-C substrate was attained through oxygen plasma pre-treatment.
- ✓ As for the device itself, the MEAs with 16 electrodes and 500 μm of diameter each, distributed over 3 mm, demonstrated an impedance of approximately 13 kΩ at 1 kHz.
- ✓ It was demonstrated that the ECoG device is easily reproducible, and it is very efficient for recording brain activity.
- ✓ High quality signals related to animal behaviour (mouse walking) were obtained, showing very high amplitudes and low noise,

References

- Buzsáki G. Large scale recording of neuronal ensembles. Nat Neurosci . 2004;7(5):446 451. **doi:10.1038/nn1233**
- Lee HB, Jin WY, Ovhal MM, Kumar N, Kang JW. Flexible transparente conducting electrodes based on metal meshes for organic optoelectronic device applications: A review. J Mater Chem C . 2019;7(5):1087 1110. **doi:10.1039/c8tc04423f**
- Machado AS, Darmohray DM, Fayad J, Marques HG, Carey MR. A quantitative framework for whole body coordination reveals specific deficits in freely walking ataxic mice. Elife . 2015; 4(OCTOBER2015):1 22. **doi:10.7554/eLife.07892**